JCB Journal of Cell Biology

ARTICLE

Structural organization of the C1a-e-c supercomplex within the ciliary central apparatus

Gang Fu[1*], Lei Zhao[2*], Erin Dymek[3], Yuqing Hou[2], Kangkang Song[1], Nhan Phan[1], Zhiguo Shang[1], Elizabeth F. Smith[3], George B. Witman[2], and Daniela Nicastro[1]

Nearly all motile cilia contain a central apparatus (CA) composed of two connected singlet microtubules with attached projections that play crucial roles in regulating ciliary motility. Defects in CA assembly usually result in motility-impaired or paralyzed cilia, which in humans causes disease. Despite their importance, the protein composition and functions of the CA projections are largely unknown. Here, we integrated biochemical and genetic approaches with cryo-electron tomography to compare the CA of wild-type *Chlamydomonas* with CA mutants. We identified a large (>2 MD) complex, the C1a-e-c supercomplex, that requires the PF16 protein for assembly and contains the CA components FAP76, FAP81, FAP92, and FAP216. We localized these subunits within the supercomplex using nanogold labeling and show that loss of any one of them results in impaired ciliary motility. These data provide insight into the subunit organization and 3D structure of the CA, which is a prerequisite for understanding the molecular mechanisms by which the CA regulates ciliary beating.

Introduction

Cilia and flagella are highly conserved organelles in eukaryotes. They have roles in cell motility, generating fluid flow, and sensing extracellular cues. Defects in ciliary assembly or function cause a wide range of human diseases, collectively termed ciliopathies (Afzelius, 2004; Fliegauf et al., 2007). The "9+2" axonemal core structure of motile cilia consists of nine outer doublet microtubules (DMTs) surrounding two singlet microtubules (C1 and C2) that form the central apparatus (CA) or central pair complex (CP). Attached to this axonemal microtubule scaffold are hundreds of proteins (Pazour et al., 2005), including the inner and outer arm dynein motors, and regulatory complexes forming part of the signal transduction pathways that coordinate dynein activity to generate ciliary motility (Summers and Gibbons, 1971; Sale and Satir, 1977; Lin and Nicastro, 2018; Witman et al., 1978; Smith and Sale, 1992; Piperno et al., 1994; Smith and Lefebvre, 1997a; Porter and Sale, 2000; Smith, 2002; Mitchell, 2004; Nicastro et al., 2006; Dymek and Smith, 2007; Wirschell et al., 2007; Bower et al., 2009; Heuser et al., 2009, 2012a,b; Yamamoto et al., 2013; Loreng and Smith, 2017; Fu et al., 2018; Kubo et al., 2018).

The CA is the largest known ciliary regulatory complex. Early structural analyses described the CA as an asymmetric assembly with seven C1 and C2 projections, but our previous cryo-electron tomography (cryo-ET) study of the WT *Chlamydomonas reinhardtii* CA revealed at least 11 projections that have 16–32-nm periodicities along the ciliary length and form connections between C1 and C2, as well as to the radial spoke (RS) heads (Witman et al., 1978; Dutcher et al., 1984; Mitchell and Sale, 1999; Mitchell, 2003; Mitchell and Smith, 2009; Carbajal-González et al., 2013; Loreng and Smith, 2017). Mutations of CA components often result in impaired or paralyzed cilia (Witman et al., 1978; Dutcher et al., 1984; Smith and Lefebvre, 1996, 1997b; Smith and Yang, 2004). Deficiency of CA proteins can cause mammalian ciliopathies, including primary ciliary dyskinesia (PCD; Teves et al., 2016; Horani and Ferkol, 2018). Mice deficient in either *Cfap54* or *Pcdp1*, which encode conserved C1d proteins, show typical PCD symptoms, including ineffective mucus clearance, male infertility, and hydrocephalus (Lee et al., 2008; DiPetrillo and Smith, 2010; McKenzie et al., 2015). Similarly, mutations of the C2b protein Hydin result in hydrocephalus caused by the loss of cilia-generated fluid flow in the brain ventricles (Lechtreck et al., 2008).

Despite many biochemical and structural studies of the CA (Witman et al., 1978; Dutcher et al., 1984; Smith and Lefebvre, 1997a; Mitchell, 2003; Mitchell and Smith, 2009; Loreng and Smith, 2017), the protein composition, 3D organization, and

[1]Departments of Cell Biology and Biophysics, University of Texas Southwestern Medical Center, Dallas, TX; [2]Department of Radiology, Division of Cell Biology and Imaging, University of Massachusetts Medical School, Worcester, MA; [3]Department of Biological Sciences, Dartmouth College, Hanover, NH.

*G. Fu and L. Zhao contributed equally to this paper; Correspondence to Daniela Nicastro: daniela.nicastro@utsouthwestern.edu; K. Song's present address is Cryo-EM Core Facility, University of Massachusetts Medical School, Worcester, MA.

functional mechanisms of the CA in ciliary motility are not fully understood. Our recent mass spectrometry (MS) study compared the proteomes of *Chlamydomonas* WT and mutant axonemes and identified 44 new candidate CA proteins assigned to the C1 or C2 microtubule (Zhao et al., 2019). However, questions about the organization, assembly, and function of the CA and its projections remain, making the CA the structurally and functionally least understood axonemal complex to date.

Here we combined biochemical, genetic, and structural analyses to investigate the protein composition and molecular organization of a group of interconnected CA projections, here termed the C1a-e-c supercomplex, in WT and CA mutants of *Chlamydomonas*. Sucrose gradient sedimentation and MS revealed that several CA proteins identified in this study, flagellar associated protein 76 (FAP76), FAP81, FAP92, and FAP216, are associated with the protein PF16, previously assigned to the C1 microtubule but not to a specific projection. *Chlamydomonas* mutants that lacked any of these proteins showed impaired motility. Structural comparisons of flagella from WT, these mutants, and tagged rescue strains revealed the precise locations of PF16, FAP76, FAP81, FAP92, and FAP216 within the C1a-e-c supercomplex. Our data show that stable assembly of this supercomplex and its interaction with the neighboring C1d projection are required for the proper regulation of ciliary motility.

Results

An improved WT CA structure

Cilia were isolated from *Chlamydomonas* cells, demembranated, and frozen rapidly for cryo-ET imaging and subtomogram averaging of the DMT and CA repeats. Our previous cryo-ET study of the WT CA structure of *Chlamydomonas* flagella achieved 3.5-nm resolution (Fourier shell correlation [FSC] 0.5 criterion; Fig. 1, A and C–E; Carbajal-González et al., 2013). Here, we improved the resolution of the CA structure to 2.3 nm (Fig. 1, B, C, F, and G) by applying advanced hardware and software. For example, tilt series were recorded with multiple frames per image (to correct for beam-induced sample motion; Brilot et al., 2012) on a direct electron detector (Cheng et al., 2015), using a Volta-Phase-Plate (to improve image contrast close to focus; Danev et al., 2014) and a dose-symmetric tilting scheme (to reduce radiation damage of the sample in images recorded at low tilt angles; Hagen et al., 2017). This improves the resolution of the subtomogram averages of axonemes, as shown by averages of DMT-associated structures with resolution as high as 1.8 nm (FSC 0.5 criterion; Lin et al., 2019).

The improved 3D structure of the *Chlamydomonas* WT CA reveals details of the CA microtubules, the bridge between them, and the various CA projections (Fig. 1, F–H; and Video 1). Previously unresolved details include (a) three filamentous structures, with a <2-nm diameter, between protofilaments 9 and 12 of the C2 microtubule (compare Fig. 1, D and F); (b) the microtubule inner protein, MIP-C2a, which forms an arch-shaped structure on the inside of the C2 wall (Carbajal-González et al., 2013; Fig. 1 E), consists of two distinct substructures that are bound to alternating tubulin subunits of protofilament 5 (Fig. 1 G); (c) the C2a projection, previously shown to have an 8-nm periodicity (Carbajal-González et al., 2013), instead has a 16-nm periodicity and adopts two conformational states (Fig. S1, A–E); (d) two connections between the C1a and C1e projections; and (e) a peripheral density at the C1c projection (Fig. S1, F and G).

A PF16-dependent complex

Our recent CA proteomics study identified several candidate C1-proteins that are reduced or absent from isolated axonemes of the *Chlamydomonas* "paralyzed flagella" mutant *pf16* (Zhao et al., 2019); these axonemes lack the entire C1 microtubule and its associated projections (Dutcher et al., 1984; Smith and Lefebvre, 1996). To identify proteins that are closely associated with the PF16 subunit, and to visualize their locations within distinct C1 projections using cryo-ET, we narrowed down the list of C1-candidate proteins to those that cosediment with PF16. Rather than comparing the cosedimentation profiles of the full axonemal proteomes between WT and *pf16*, we limited the proteome of interest by comparing the *pf28* mutant, which lacks the large outer dynein arm complexes but contains the CA (Mitchell and Rosenbaum, 1985; Kamiya, 1988), with the double mutant *pf28; pf16*. The isolated axonemes were extracted using high potassium iodide (KI) concentration, which eliminates the DMTs and proteins strongly associated with the DMTs from the sample. The KI extracts were separated on sucrose gradients under native conditions.

We probed the sucrose gradient fractions of the *pf28* extract with anti-PF16 antibody, analyzed the positive fractions with MS, and subtracted those proteins that were also found in comparable fractions of the C1-less double mutant *pf28;pf16* (Table S1). Cross-referencing the proteins of this difference set with previous studies identified 16 potential PF16-associated proteins (Table 1): five proteins (PF6, FAP101, FAP114, FAP119, and FAP227) were previously assigned to the C1a projection and two (FAP221 and FAP54) to the C1d projection, whereas PP1c (Yang et al., 2000) and eight recently identified candidate C1 proteins (Zhao et al., 2019) had not yet been assigned to specific C1 projections. Of these nine unassigned proteins, FAP76, FAP81, FAP92, and FAP216 were large enough to be suitable targets for cryo-ET imaging. *Chlamydomonas* mutants corresponding to FAP76 (*fap76-1* and *fap76-2*), FAP81, FAP92, and FAP216 were purchased from the *Chlamydomonas* Library Project (CLiP; https://www.chlamylibrary.org; Li et al., 2016). Mutations were verified by PCR (Fig. S2 A) and MS (Table 1), and rescue of the mutant phenotypes (motility and structure), by transformation with the corresponding WT genes. We also generated a *fap76-1; fap81* double mutant.

PF16, a C1a projection subunit, is required for C1a-e-c complex assembly

A previous conventional EM study showed that in the *pf16* mutant, the C1 microtubule and its projections were unstable upon isolation of axonemes, i.e., only 8% of *pf16* axonemes contained the C1 and C2 microtubules (9+2 axonemes), whereas most of the intact *pf16* flagella had both CA microtubules, as did flagella and isolated axonemes from WT *Chlamydomonas* (Dutcher et al., 1984; Mitchell and Sale, 1999). However, the resolution in

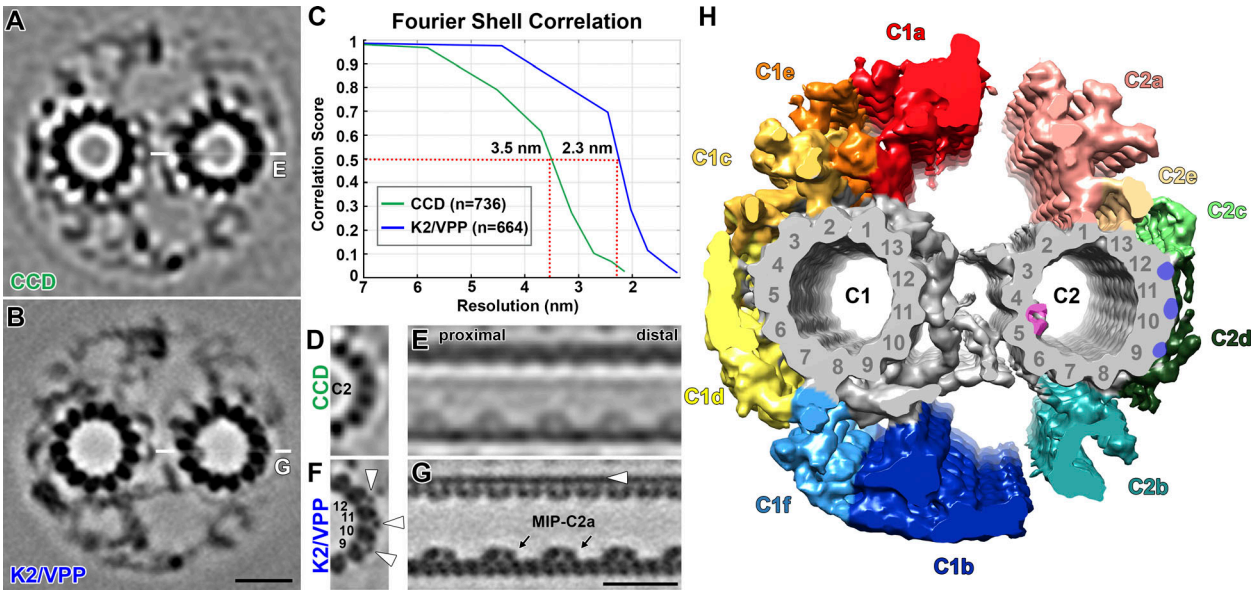

Figure 1. **Improved resolution of the averaged CA structure. (A and B)** Tomographic slices of the averaged 32-nm repeat of the *Chlamydomonas* WT CA viewed in cross section to compare data recorded with either a CCD camera (A) or a direct electron detector and Volta Phase Plate (K2/VPP; B). Thin white lines in A and B indicate the locations of the slices shown in E and G, respectively. **(C)** FSC curves of the CA averages show that the resolution is improved from 3.5 nm for CCD data to 2.3 nm for K2/VPP data (0.5 criterion). **(D–G)** Tomographic slices to compare the C2 microtubule-associated structures between the CCD (D and E) and the K2/VPP data (F and G) in cross-sectional (D and F) and longitudinal (E and G) views. Note the clear visualizations of (a) filamentous, microtubule-associated proteins between protofilaments 9–12 (white arrowheads in F and G), (b) two distinct domains of the microtubule inner protein (MIP) C2a (black arrows in G), and (c) the tubulin lattice of the microtubule wall (G) in the K2/VPP data, which were not observed or were blurred in the CCD data. **(H)** Isosurface rendering shows the averaged *Chlamydomonas* WT CA (K2/VPP data) in cross-sectional view. Naming and coloring of CA projections adopted from Mitchell and Sale (1999) and Carbajal-González et al. (2013). CA protofilaments were not previously numbered; here we assigned protofilament #1 of C1 and C2 to where the C1a and C2a projections attach, respectively. In all figures, cross sections are viewed from proximal (i.e., cell body) to the ciliary tip, and in longitudinal views the proximal side is on the right (except for Fig. 1, E and G; and Fig. S1, A–E). Scale bar in B, 20 nm (valid for A and B); in G, 20 nm (valid for D–G).

previous studies was insufficient to visualize the extent of missing C1 projections in *pf16* axonemes containing the C1 microtubule. Therefore, to characterize the CA structure that requires PF16 protein for its stable assembly, we performed cryo-ET and subtomogram averaging of those *pf16* CAs that still contained a C1 microtubule (9+2) and compared the averages to the WT CA structure. Of 39 cryo-tomograms of *pf16* axonemes, only 10% had both microtubules (9+2), whereas the remaining axonemes lacked either the C1 microtubule (9+1, 51%) or the entire CA (9+0, 39%), consistent with previous studies (Dutcher et al., 1984; Mitchell and Sale, 1999). The subtomogram averages revealed that in the *pf16* 9+2 axonemes, the C1d, C1f, and C1b projections remained structurally intact, and only the C1a, C1e, and C1c projections, with an estimated total mass of ∼2.0 MD, were absent (Fig. 2, E–H; for consistency, we follow the previous nomenclature for CA projections [Carbajal-González et al., 2013]). Thus, the C1a-e-c projections require PF16 for stable assembly onto the C1 microtubule, and they form a protein interaction network suggestive of a "C1a-e-c supercomplex" within the ciliary CA.

Although the structural defect in the *pf16* mutant was informative about the extent of the PF16-dependent protein network, it did not reveal the location of the PF16 protein within the C1a-e-c supercomplex. To determine the location of PF16, we used the clonable biotin carboxyl carrier protein (BCCP) tag, developed for visualizing gene products by cryo-ET, and subtomogram averaging (Oda and Kikkawa, 2013; Song et al., 2015). We rescued the *pf16* mutant with WT *PF16* C-terminally tagged with BCCP. Axonemes of the rescued strain were isolated, and the biotinylated tag was enhanced with streptavidin-nanogold, which is visible as additional cryo-EM density in comparison with the WT structure (Song et al., 2015; Fu et al., 2018). Tomograms of the *pf16;PF16::BCCP* rescue showed only 9+2 axonemes, and all CA projections were restored to the WT architecture with and without (control) addition of streptavidin-gold (Fig. 2, I–P), confirming that stable assembly of the C1 microtubule and C1a-e-c supercomplex requires PF16 protein. In contrast to the WT (Fig. 2, A–D) and control axonemes without streptavidin-gold (Fig. 2, I–L), the CA average of *pf16;PF16::BCCP* with streptavidin-gold revealed an additional cryo-EM density in the periphery of the C1a projection (blue arrowheads in Fig. 2, M–P; and Video 2), indicating the location of the PF16 C-terminus.

We were unable to rescue the *pf16* mutant with N-terminally tagged PF16, possibly because the PF16 N-terminus is required for protein–protein interactions and assembly of the C1a-e-c supercomplex, or the N-terminal BCCP tag (9 kD) disrupts PF16 folding or its transport into the axoneme.

C1a-e-c supercomplex mutants have defective swimming and photoshock response

CA mutants often have paralyzed flagella (see *pf16* in Fig. 3 A). In contrast, the *fap76-1*, *fap81*, *fap92*, and *fap216* cells swim, but with

Table 1. **MS analysis of the proteins associated with the PF16-related complex within the ciliary CA**

Protein	Molecular weight (kD)	Phytozome gene number	Unique peptides in different strains (n)[a]						Quantification ratio[a]				
			WT	*pf16*	*fap76-1*	*fap81*	*fap92*	*fap216*	*pf16*/WT	*fap76-1*/WT	*fap81*/WT	*fap92*/WT	*fap216*/WT
Proteins traditionally assigned to the C1 microtubule[b]													
PF16 (C1)	50	Cre09.g394251	25	**0**	21	26	26	**27**	**0**	0.86	0.89	1.18	1.08
PF6 (C1a)	237	Cre10.g434400	99	**47**	98	103	107	100	**0.03**	0.57	0.95	1.09	1.02
FAP101/C1a-86 (C1a)	86	Cre02.g112100	24	**7**	24	25	23	24	**0.02**	0.72	0.61	1.17	0.93
FAP119/C1a-34 (C1a)	34	Cre06.g256450	13	8	11	12	13	13	**0.04**	0.54	0.73	1.4	1.01
FAP114/C1a-32 (C1a)	32	Cre09.g389282	16	**6**	16	15	17	15	**0.08**	0.84	0.6	0.91	0.98
FAP227/C1a-18 (C1a)	20	Cre17.g729850	17	**6**	17	17	16	18	**0.04**	1.08	0.6	0.96	0.96
PP1C (C1)	35	Cre06.g292550	14	9	15	14	15	13	0.2	0.52	0.94	0.96	0.28
FAP221 (C1d)	104	Cre11.g476376	40	36	38	40	45	45	0.47	0.67	1.05	1.17	0.84
FAP54 (C1d)	318	Cre12.g518550	108	80	95	119	106	115	0.36	0.54	1.13	0.92	0.92
Novel PF16-associated proteins[c]													
FAP76	162	Cre09.g387689	60	**22**	**11**	52	64	63	**0.05**	**0**	0.72	0.89	1.09
FAP81	172	Cre06.g296850	54	**2**	50	**0**	56	52	**0**	0.49	**0**	1.3	1.01
FAP92	150	Cre13.g562250	51	**5**	41	38	50	52	**0**	0.31	0.37	0.88	1.03
FAP216	79	Cre12.g497200	23	**2**	21	**5**	24	**0**	**0**	0.69	**0.07**	1.14	**0**
FAP105	31	Cre12.g511750	27	**0**	29	27	28	27	**0**	0.87	1.07	1.23	1.24
FAP108	22	Cre06.g297200	11	11	8	11	12	11	0.79	9.98	0.87	0.77	1.63
FAP305/MOT17	28	Cre11.g482300	12	12	12	13	13	11	**0.06**	0.59	2.44	1.65	0.77
FAP412	57	Cre12.g497450	24	**0**	29	24	25	24	**0**	0.71	1.24	1.38	0.99

[a]Missing or significantly reduced unique peptide numbers (less than half of WT) or ratios (<0.2) are highlighted in bold; MS analysis of *pf16* and *fap76-1* was originally from Zhao et al. (2019); quantification ratios of *pf16*/WT and *fap76-1*/WT were estimated by the IBAQ method (Schwanhäusser et al., 2011); *fap81*/WT, *fap92*/WT, and *fap216*/WT were estimated by the MIC sin value (Trudgian et al., 2011).
[b]Proteins traditionally assigned to the C1 microtubule in general (C1) or specifically to the C1a or C1d projection, as indicated.
[c]Proteins that were identified in sucrose gradient analyses of *pf28* and *pf28;pf16* samples and also predicted to be associated with C1 (Zhao et al., 2019) are included here.

slower velocity and a curving swimming path, caused by lack of synchronization between the two flagella (Video 3), rather than the straight or loose helical paths of WT cells (Fig. 3, A and B; and Video 3). Among the four mutants, *fap92* has the mildest motility impairment (70% WT swimming speed and only a slight curving path). Cells from *fap76-1*, *fap81*, *fap216*, and the double mutant *fap76-1;fap81* have similarly severe motility defects, with slower velocity (~50% of WT) and clearly curving swimming paths (Fig. 3, A and B). Flagella asynchrony has also been reported for a *Chlamydomonas fap74* RNAi mutant that lacks the C1d projection (DiPetrillo and Smith, 2011).

Previous studies have shown that C1d-less mutants lack a proper photoshock response (DiPetrillo and Smith, 2011; Brown et al., 2012). Our results show that the photoshock response is also impaired in the C1a-e-c supercomplex CLiP mutants, i.e., only 35%, 6%, 7%, and 5% of *fap76-1*, *fap81*, *fap216*, and double mutant *fap76-1;fap81* cells, respectively, exhibited photoshock, whereas *fap92* had a milder photoshock defect (81%; Fig. 3 C). The WT swimming speed and straight swimming path were completely restored in the rescue strains *fap76-1;BCCP::FAP76* and *fap216;BCCP::FAP216* (Fig. 3, A and B); however, the photoshock response of *fap76-1;BCCP::FAP76* was still slightly impaired (72%; Fig. 3 C). The similar phenotypes of the C1a-e-c and previously reported C1d mutants suggest that these CA projections might functionally interact to regulate ciliary motility.

Subunit localization within specific CA projections

The impaired cell motility and the perturbed proteome of the C1a-e-c supercomplex mutants suggest defects in their flagellar structure. Therefore, we used cryo-ET and subtomogram averaging to compare the CLiP mutant CA and control DMT structures with WT axonemes. None of the mutant averages showed DMT-associated defects (Fig. S3, A–G), but all of them revealed structural defects in the CA, with a loss of mass ranging from 80 kD to 1.2 MD.

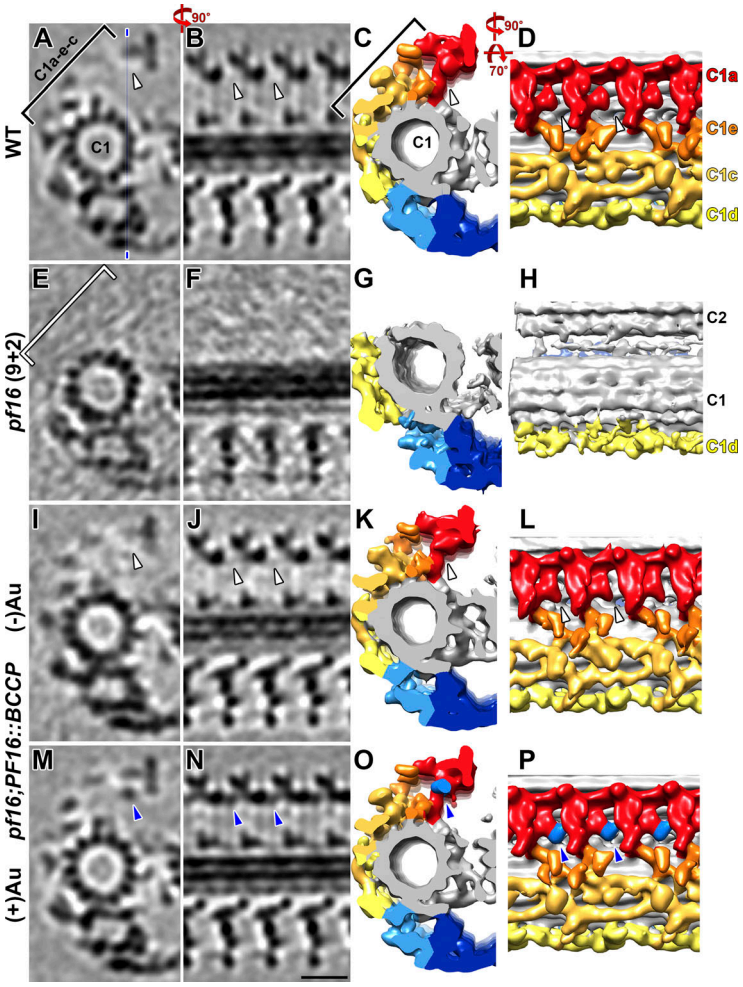

Figure 2. **CA projections C1a, e, and c are lost in the *pf16* mutant, and the PF16 C-terminus locates to the C1a projection. (A–P)** Tomographic slices (columns 1 and 2) and isosurface renderings (columns 3 and 4) of the averaged CA repeats of WT (A–D), 9+2 *pf16* (E and F), and the tagged rescue *pf16;PF16::BCCP* without adding nanogold (I–L, control) and after treatment with streptavidin gold (M–P) in cross-sectional (columns 1 and 3) and longitudinal views (columns 2 and 4). The thin blue line in A indicates the location of the slices shown in column 2. The C1a, e, and c projections (indicated by black brackets in A and C) were missing in the *pf16* mutant (white bracket in E). When the C-terminus of PF16 was tagged with BCCP, the additional density of the BCCP-streptavidin-gold label was detected in the C1a projection (blue arrowheads in M–P); this label density was not observed in WT (white arrowheads in A–D) or control samples (white arrowheads in I–L). Scale bar in N, 20 nm (valid for all EM images).

FAP92 is a C1a protein that connects neighboring C1a projections

Compared with WT, the *fap92* CA is missing a sheet-like C1a density (compare Fig. 3, D–G with H–K; and Video 2). In the WT CA, this sheet-like structure has a 16-nm periodicity along the axonemal length and contributes to the connection between neighboring C1a projections in the periphery of the CA (Fig. 3 G). The MS analyses identified similar numbers of unique peptides throughout the predicted amino acid sequence of FAP92 in both WT and *fap92* axonemes, suggesting that FAP92 is present in isolated *fap92* axonemes (Table 1). However, sequencing of the genomic DNA showed that the cassette was inserted into the 13th exon of *FAP92* in the mutant genome (Fig. S2 A), which was accompanied by the deletion of three nucleotides (ACC) immediately upstream of the insertion site in exon 13 (unpublished data). The remainder of exon 13 was intact downstream of the cassette. RT-PCR confirmed that the coding region of *FAP92* was disrupted, with a fragment corresponding to exons 12–15 being amplified from WT but not from *fap92* cDNA (Fig. S2 B).

The mutant FAP92 protein structure is likely altered, causing it to be partially disordered or positionally flexible and thus not visible in the axonemal averages, and/or precluded from forming stable interactions with FAP413, which was significantly reduced in *fap92* axonemes (Table S2). The remaining C1a structures are not destabilized in the *fap92* mutant (e.g., the classification analyses did not reveal structural flexibility of the C1a projections), and neighboring C1a projections are still connected through additional linking structures (Fig. 3 K), even though *fap92* cells swim slowly, indicative of impaired flagellar motility. Thus, FAP92 probably has a role in regulating ciliary beating, as opposed to having a major scaffolding function.

FAP76 is a C1c protein that interacts with the C1e and C1d projections

Cryo-ET and subtomogram averaging of the *fap76-1* mutant revealed that the outer part of the C1c projection was missing in the mutant CA compared with WT (compare Fig. 4, A–D with E–H). The FAP76-dependent density (magenta in Fig. 4 I) has a triskelion-like shape with 32-nm periodicity along the C1 microtubule. MS analysis of *fap76-1* axonemes revealed that FAP76 is significantly reduced (Table 1), and the estimated size of the triskelion-shaped density of ∼190 kD suggests it contains a single copy of FAP76 (170 kD). FAP76 forms at least three connections with neighboring structures involving three different CA projections: #1 is the interaction between FAP76 and other C1c densities near the interface between the C1c and C1e projections (Fig. 4 I and Video 2); #2 is the attachment of FAP76 to a rod-shaped C1d density; and #3 links two C1d projections (Fig. 4 J and Video 2).

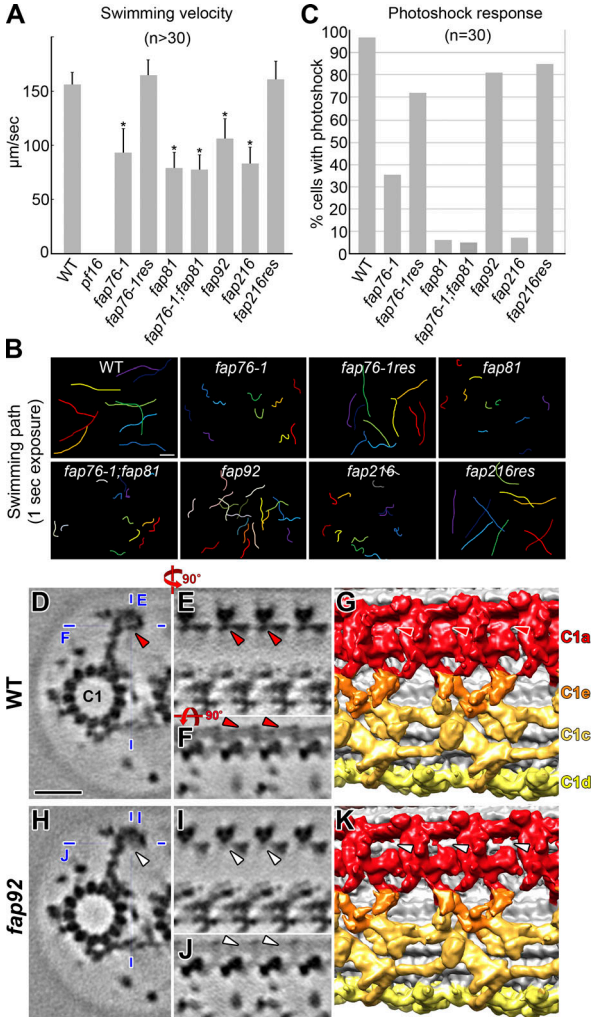

Figure 3. **Motility defects of C1a-e-c mutants, and FAP92 is a C1a protein. (A)** Average swimming velocities of WT and mutant cells and rescue strains *fap76-1;BCCP::FAP76* (*fap76-1res*) and *fap216;BCCP::FAP216* (*fap216res*). In the sequence as shown in the histogram n = 30, 30, 30, 30, 30, 30, 32, 40, and 34. *, Significant difference (Student's t test, $P < 0.01$) compared with WT. Error bars indicate ± SEM. **(B)** Each colored line represents the swimming path of one cell recorded for 1 s. The swimming paths of mutants are curving. **(C)** The percentage of cells displaying photoshock response, i.e., that switched from forward swimming to backward swimming upon light stimulus, compared with WT. **(D–K)** Comparisons of tomographic slices (D–F and H–J) and isosurface renderings (G and K) between the averaged CA repeats of WT (D–G) and *fap92* axonemes (H–K) viewed in cross-sectional (D and H), longitudinal (E, G, I, and K) and top-down (F and J) orientations, showing a sheet-like density that is present in the WT C1a projection (red arrowheads in D–G) but missing in *fap92* (white arrowheads in H–K). Thin blue lines indicate the location of the tomographic slices shown in E and F (in D) and I and J (in H). Scale bar in B (WT), 50 μm (valid for all images in B); D, 20 nm (valid for D–F and H–J).

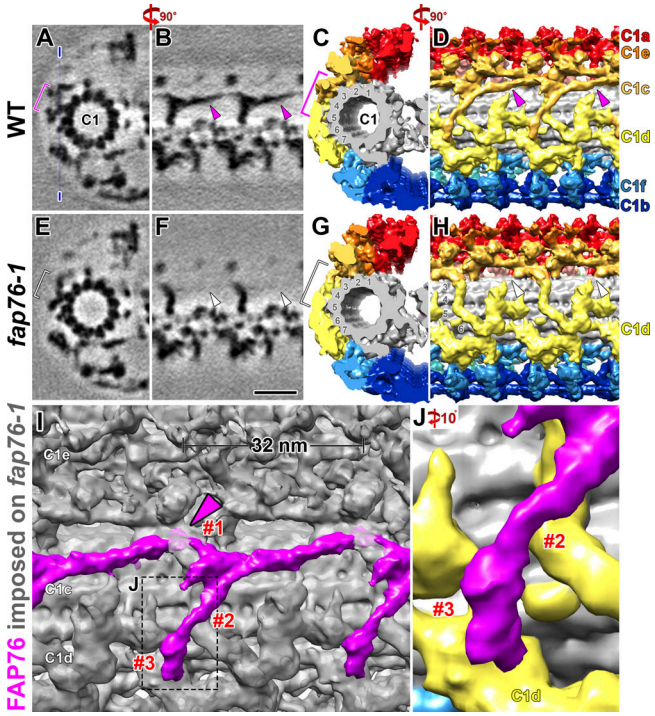

Figure 4. **FAP76 is a C1c protein with multiple connections to neighboring structures. (A–H)** The comparison of tomographic slices (A, B, E, and F) and isosurface renderings (C, D, G, and H) between the averaged CA repeats of WT (A–D) and *fap76-1* axonemes (E–H) viewed in cross-sectional (A, C, E, and G) and longitudinal (B, D, F, and H) orientations shows a triskelion-shaped structure that is present in the WT C1c projection (magenta brackets and arrowheads in A–D) but missing in *fap76-1* (white brackets and arrowheads in E–H). The thin blue line in A indicates the location of the tomographic slices shown in B and F. **(I and J)** The isosurface rendering of a difference map between the averaged CA of WT and *fap76-1* shows the triskelion-shaped FAP76 densities (magenta) in longitudinal view superimposed on the averaged CA of *fap76-1* (gray) in overview (I) and zoomed-in (J, location indicated by box in I). Note the three connections (magenta arrowhead and #1–3) of FAP76 with neighboring structures, i.e., #1 with the C1c projection close to C1e (I), and #2 and #3 with C1d densities (yellow in J). Scale bar in F, 20 nm (valid for A, B, E, and F).

The FAP76 density consists of a 32-nm-long filamentous part and a thicker "branch" extending from the middle of the filament to connection #1 (Fig. 4 I). To analyze the FAP76 structure, we rescued *fap76-1* with N-terminally BCCP-tagged FAP76. Rescue cells swim (mostly) with WT motility (Fig. 3, A–C). Using immunofluorescence microscopy and SDS-PAGE, we confirmed that BCCP-FAP76 assembled into the axonemes of the rescued cells (Fig. 5, A and B). In the subtomogram averages of *fap76-1;BCCP::FAP76* axonemes labeled with streptavidin-nanogold, we found an additional density where the short "branch" of FAP76 connects to the C1e projection (Fig. 5, J–L, blue arrowheads), indicating the location of the FAP76 N-terminus. This additional density was not visible in WT axonemes or *fap76-1;BCCP::FAP76* without streptavidin-nanogold (Fig. 5, D–I, white arrowheads). Although the overall CA structure of *fap76-1;BCCP::FAP76* resembles that of WT, one of the two globular-shaped structures at the C1c-e junction (C1c peripheral subunit 1 [psu1] and black arrow in Fig. 5, E and F) appears to be missing with and without incubation with streptavidin-Au (white arrow in Fig. 5, H, I, K, and L). A classification analysis focused on C1c psu1 revealed that ∼40% of WT and ∼38% of *fap76-1* CA repeats, but <10% of CA repeats in the *fap76-1;BCCP::FAP76* rescued strain, contained the C1c psu1 structure (Fig. 5). The close proximity of the FAP76 N-terminus to this subunit suggests that the BCCP tag in the rescue strain might disrupt assembly of the globular subunit.

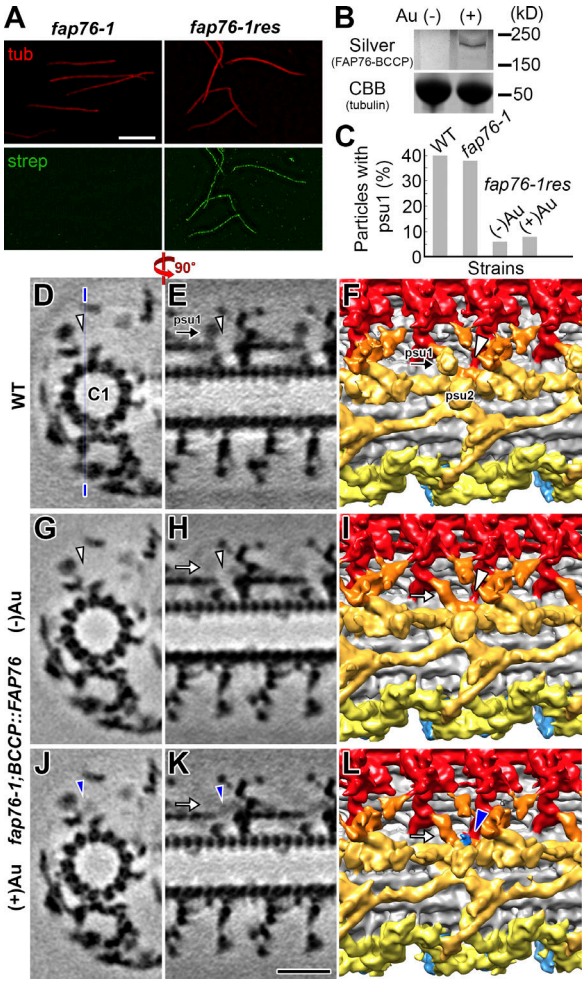

Figure 5. **The FAP76 N-terminus is located at the interface between C1c and C1e projections. (A)** Immunofluorescence light microscopy images of axonemes isolated from *fap76-1* (left) and *fap76-1;BCCP::FAP76* rescue (right) probed by anti-acetylated-tubulin antibody (red) and fluorescently tagged streptavidin (green). The streptavidin signal indicates that the BCCP-tagged FAP76 was assembled into the axoneme of the rescued strain. **(B)** SDS–polyacrylamide gel stained by a silver enhancement kit (top) to show that a specific band of appropriate relative mobility could be detected in the *fap76-1;BCCP::FAP76* axonemes treated with streptavidin-Au, but not in the control (–Au). Coomassie brilliant blue (CBB) staining (bottom) shows the tubulin bands as loading controls. **(C)** A classification analysis of the C1c psu1 (black arrows in E and F) in WT and *fap76-1*, and *fap76-1;BCCP::FAP76* rescue axonemes (white arrows in H, I, K, and L). The particle numbers (n) included in the averages for WT, *fap76-1*, *fap76-1;BCCP::FAP76* (+Au), and *fap76-1;BCCP::FAP76* (–Au) were 664, 927, 1,089, and 935 (see Table S3). **(D–L)** Comparison of tomographic slices (D, E, G, H, J, and K) and isosurface renderings (F, I, and L) of the averaged CA repeats of WT (D–F) versus *fap76-1;BCCP::FAP76* rescue strain either without (G–I) or treated with (J–L) streptavidin gold, viewed in cross-sectional (D, G, and J) and longitudinal (E, F, H, I, K, and L) orientations. The additional density of the streptavidin-gold label at the interface between the C1c and C1e projections in the gold-treated rescue strain (blue arrowheads in J–L) is not observed in WT or control CA (white arrowheads in D–I). Thin blue line in D indicates the location for the tomographic slices shown in E, H, and K. Scale bar in A, 5 µm (valid for all fluorescence images); K, 20 nm (valid for all EM images in D–L).

This defect might also explain the partial rescue of the photoshock response in *fap76-1;BCCP::FAP76* (Fig. 3 C). Comparisons of the proteomes of WT, *fap76-1* (Table 1), and *fap76-1;BCCP::FAP76* (not depicted) did not reveal missing proteins that might correspond to C1c psu1, suggesting that C1c psu1's apparent absence in the tomogram averages of the latter strain is due to positional flexibility that occurs when FAP76 is replaced with FAP76-BCCP.

We also analyzed a second CLiP mutant, *fap76-2*, in which the *FAP76* gene was disrupted by insertion of the cassette at a location closer to the 3′ end of the gene than in *fap76-1* (Fig. S4 A). The phenotype of *fap76-2* is very similar to that of *fap76-1* with regard to both motility (Fig. S4, B–D) and structural defects (Fig. S4, F and G). In contrast to *fap76-1*, MS analysis of *fap76-2* showed that a truncated FAP76 protein is assembled into the *fap76-2* axoneme, and that levels of two more proteins, DPY30 and FAP380, are reduced compared with *fap76-1* (Fig. S4, E–G). Competition with this truncated FAP76 protein could explain our observation that FAP76-HA expression in *fap76-2* results in only a partial rescue of motility (unpublished data), whereas *fap76-1* is completely rescued (Zhao et al., 2019).

FAP81 is required for stable assembly of the C1e and C1c projections

The *fap81* CA had the most severe structural defects of the four CLiP mutants. The WT versus mutant comparison revealed that the C1e and C1c projections were missing in the averaged *fap81* CA repeat (compare Fig. 6, A–C with D–F; and Video 2), indicating that FAP81 is required for stable assembly of the C1e-c subcomplex. The estimated size of the WT C1e-c subcomplex is 1.2 MD. However, MS and Western blot analyses of *fap81* axonemes revealed that, of the 16 proteins associated with PF16, only FAP81 (172 kD) and FAP216 (79 kD) were substantially reduced (Table 1 and Fig. S2 D). This suggests that some of the C1e-c proteins might still bind to the *fap81* axoneme but cannot be visualized in the averaged *fap81* CA due to partial reduction and/or positional flexibility. This is supported by the observation that in the region where FAP76 connects to the C1d projection (#3 connection, Fig. 4 I), a weak FAP76 density remained visible in the averaged *fap81* CA, whereas this density was missing in *fap76-1* and *fap76-1;fap81* (compare Fig. S5, A and C with B and D). A classification analysis focused on this region could clearly visualize the part of FAP76 that connects to the C1d projections in more than half of the *fap81* CA repeats (compare Fig. S5, E and F), which is consistent with MS data showing that a considerable number of FAP76 peptides were detected in the *fap81* axonemes (Table 1). Nonetheless, large parts of FAP76, including its N-terminal region, remained undetectable even in the class averages of *fap81*. This suggests that FAP81 interacts with the N-terminal part of FAP76, and without this interaction FAP76 becomes positionally flexible. Despite the partially remaining FAP76 protein in *fap81*, the similar phenotypes of *fap81* and *fap76-1;fap81* indicate that the positionally flexible FAP76 did not function properly in *fap81* axonemes.

Comparison of the WT and *fap81* CAs allowed a more precise characterization and delineation of the C1a and C1e densities. In WT, the C1a projection, which repeats every 16 nm, has multiple interaction sites with the C1e projection, which repeats every 32 nm (Fig. 6 G). Our data clearly showed that alternating C1a

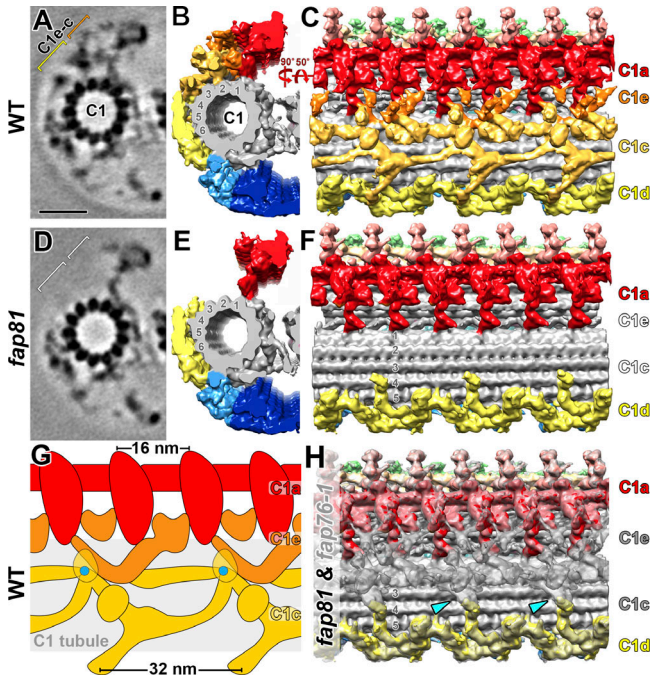

Figure 6. **FAP81 is required for the stable assembly of the C1e-c subcomplex. (A–F)** Comparison of tomographic slices (A and D) and isosurface renderings (B, C, E, and F) between the averaged CA repeats of WT (A–C) and *fap81* (D–F), viewed in cross-sectional (A and D) and longitudinal (B, C, E, and F) orientations, shows that the C1e and C1c projections (orange/yellow brackets in A) are present in WT but missing in *fap81* (white bracket in D). **(G)** Schematic drawing of the WT CA structure in longitudinal view to outline the densities of the C1a (red) and C1e (orange) projections and their interactions. Note the transition from 16-nm periodicity (C1a) to 32-nm periodicity (C1e). Blue dots indicate the locations of the FAP76 N-terminus. **(H)** An overlay of the averaged CA repeats of *fap76-1* (transparent gray) and *fap81* (colored) shows the interaction (cyan arrowheads) between a rod-shaped C1d density and the gray C1c density, which remains present in the *fap76-1* CA and consists of at least the FAP81 protein. Scale bar in A, 20 nm (valid for A and D).

projections interact with different parts of each C1e projection (Fig. 6 G). The results for *fap81* also provided insight into the interactions between FAP81 and C1d. Since FAP81 is not significantly reduced in *fap76-1* axonemes (Table 1), the remaining C1c densities in *fap76-1* are likely composed of FAP81 and FAP216. Comparison of *fap81* with *fap76-1* reveals that FAP81 interacts with a rod-shaped C1d density that is anchored to C1 protofilament 4 (Fig. 6 H).

FAP216, a C1c subunit, links the C1 microtubule and peripheral C1c projection densities

Our MS analyses revealed that, in addition to FAP81, FAP216 was significantly reduced in *fap81* axonemes, whereas FAP81 was present at WT level in *fap216* (Table 1). This suggests that the assembly of FAP216 into the axoneme requires FAP81 but not vice versa. Structural analysis of *fap216* showed that two small densities were missing or reduced in the C1c and C1e projections (Fig. 7, E–H, light orange and white arrowheads). In the WT CA, the affected C1c structure links the more peripheral C1c projection density to the C1 microtubule between protofilaments 2 and 3 (Fig. 7, A–D, yellow arrowheads). The estimated molecular mass of the affected C1c density is ∼90 kD, suggesting that this density is composed of a single copy of FAP216 (79 kD). The affected C1e density, which forms a bridge between the C1c and C1a projections in WT (orange arrowhead in Fig. 7, A and C), is only partially reduced in *fap216* (light orange arrowhead in Fig. 7, E and G), and classification analysis revealed that this C1e density was missing in only 57% of the *fap216* CA repeats (Fig. S5, G–J). This, together with the results of the MS analyses, which did not detect any FAP216 peptides in *fap216* axonemes, indicates that the partial reduction of this density is likely a secondary defect. The proteins corresponding to the reduced C1e density could not be identified by our MS comparisons between WT and *fap216* mutant axonemes.

Although the structural CA defects in *fap216* are considerably less severe than those of *fap81*, both mutants display equally severe swimming defects. We also showed that transformation of *fap216* with the WT gene for FAP216 is sufficient to restore the WT phenotype (Fig. 3, A–C). Classification analyses of the *fap216* CA focused on the areas neighboring the structural defects did not reveal any positional flexibilities of the remaining densities, i.e., FAP216 does not appear to play a critical role in the stable assembly of the remaining C1a-e-c protein network. Instead, these results suggest that FAP216 is an essential component in a signal transduction cascade that regulates ciliary motility in *Chlamydomonas*.

Discussion

Composition and hierarchical assembly of the C1a-e-c supercomplex

Our WT versus mutant comparisons have revealed a 2-MD PF16-associated protein network, the C1a-e-c supercomplex, within the ciliary CA. We show that PF16 is potentially associated with ≥16 proteins (Table 1) with a combined molecular mass of 1.6 MD, suggesting that multiple protein copies and/or additional proteins form the supercomplex. Our MS analyses also identified two proteins, FAP54 and FAP221, previously assigned to C1d, among the PF16-associated proteins, suggesting that they have stable attachments to C1a-e-c supercomplex proteins. Such strong interaction between the C1c and C1d projections is consistent with the observed structural connections.

We characterized mutant phenotypes and the molecular organization for five C1a-e-c supercomplex proteins. PF16 and FAP92 are C1a projection proteins, whereas FAP76, FAP81, and FAP216 are the first identified C1e and C1c proteins (Table 1, Fig. 8, and Video 2). The CA structural defects in the mutants suggest hierarchical assembly of the C1a-e-c supercomplex. The complex was disrupted in *pf16* axonemes, suggesting that the C1a protein PF16 is a crucial scaffold protein required for stable assembly of the entire supercomplex (Figs. 2 and 8). Loss of PF16, and the supercomplex, destabilizes the entire C1 microtubule and associated projections, as only ∼10% of the *pf16* axonemes had 9+2 axonemes.

The second largest supercomplex defect was observed in *fap81* axonemes, suggesting that FAP81 is essential for stable assembly of the C1e-c subcomplex that consists of at least FAP76, FAP81, and FAP216. In contrast, the single loss of FAP76, FAP92,

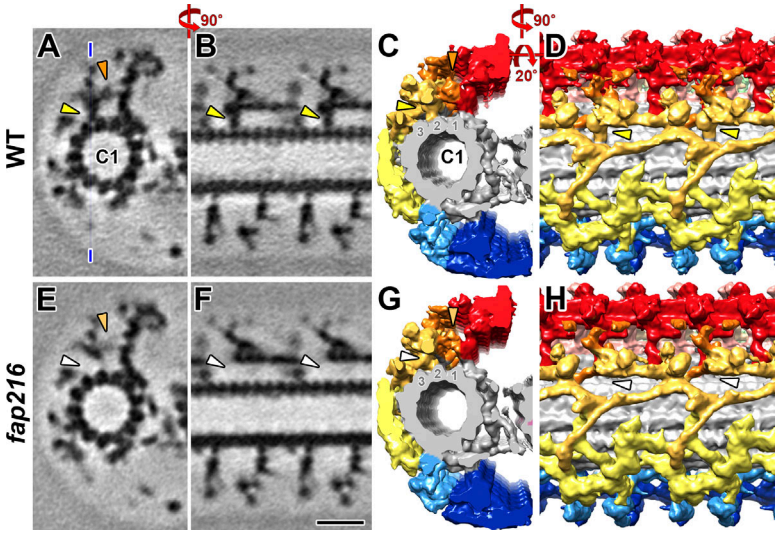

Figure 7. **FAP216, a C1c protein that may bridge the C1 microtubule and peripheral C1c densities. (A–H)** Comparisons of tomographic slices (A, B, E, and F) and isosurface renderings (C, D, G, and H) between averaged CA repeats of WT (A–D) and *fap216* (E–H) viewed in cross-sectional (A, C, E, and G) and longitudinal (B, D, F, and H) orientations shows that the *fap216* CA lacks a small C1c density (white arrowheads in E–H) that in WT connects between C1 microtubule protofilament 2 and peripheral C1c densities (yellow arrowheads in A–D). In addition, part of the C1e projection (orange arrowheads in A and C) that bridges between the C1e-c subcomplex and the C1a projection is reduced in *fap216* (light orange arrowhead in E and G). Classification analysis confirmed that 57% of the *fap216* CA repeats lack this C1e density (see Fig. S4). Scale bar in F, 20 nm (valid for all EM images).

or FAP216 had minimal effects on the assembly of other C1a-e-c supercomplex components. Despite at least two FAP76 contact sites and one FAP81 contact site to C1d projection densities (Figs. 4 and 6), none of the mutants showed defects in C1d projection assembly. Likewise, classic thin-section transmission EM (TEM) of two C1d-defective mutants, *fap46* and FAP74 RNAi, which lack the entire C1d projection, showed no obvious effects in structures corresponding to the C1a-e-c supercomplex (DiPetrillo and Smith, 2010; Brown et al., 2012). Our precise localization of FAP76, FAP81, FAP92, and FAP216 within the C1a-e-c supercomplex agrees well with the recent assignment for these proteins to the C1 microtubule (Zhao et al., 2019). In our previous study (Zhao et al., 2019), FAP81 was found to immunoprecipitate with known C1a/e proteins, but it could not be definitively assigned to either of these projections. This highlights that the integration of biochemical and structural data are critical for a comprehensive understanding of the molecular architecture of the CA.

Supercomplex subunits form connections within the complex and with the C1d projection

The improved resolution of our cryo-ET data revealed that the C1a-e-c supercomplex makes three connections with the neighboring C1d projection and multiple interactions within the

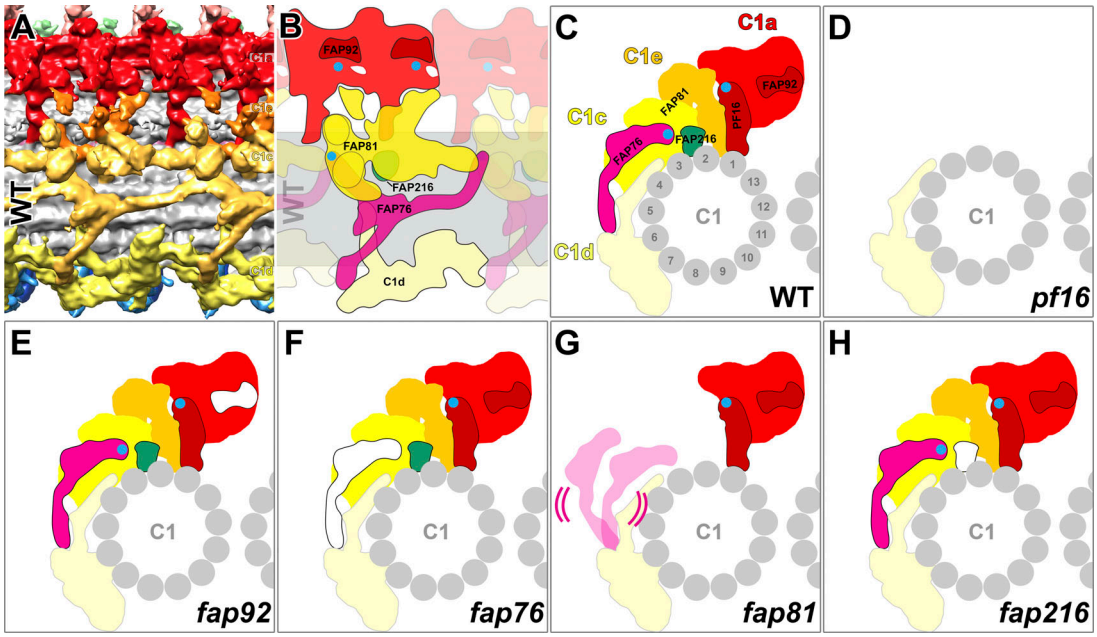

Figure 8. **Models of the C1a-e-c supercomplex. (A)** The isosurface rendering shows the 3D structure of the averaged *Chlamydomonas* WT CA repeat viewed in longitudinal orientation. **(B and C)** A schematic drawing of the 32-nm repeat of the *Chlamydomonas* WT CA in longitudinal orientation (B; same orientation as in A) and cross-sectional view (C) to highlight the protein compositions of the C1a-e-c supercomplex within the ciliary CA; this includes densities containing the subunits PF16 and FAP92 (dark red), FAP76 (magenta), FAP81 (yellow), and FAP216 (green). Blue dots indicate the C-terminus of PF16 and N-terminus of FAP76 proteins. **(D–H)** Schematic drawings of the 32-nm CA repeat of various C1a-e-c mutants in cross-sectional view to show the observed structural defects.

complex, such as the interface between the C1a and C1e projections, where the structural periodicity transitions from 16 nm (C1a) to 32 nm (C1e; Fig. 6 G). Alternating C1a projections, which physically interact with each other, have different connections to each C1e projection, suggesting that the alternate C1a projections could have distinct functions.

The C1a projection is anchored to C1 protofilament 1, with 16-nm periodicity (Figs. 2 C and 6 E), which might involve the N-terminal domain of PF16 (Fig. 8). Every 16 nm, the C1e-c subcomplex has two adjacent connections to C1 protofilament 2. The smaller connecting density consists of FAP216 (yellow arrowheads in Fig. 7, A–D) and did not appear essential for complex docking, whereas the larger distal connection is a protein interaction hub involving multiple structures, including C1e, the C1c psu1 and psu2, FAP81, and the N-terminal domain of FAP76 (#1 connection, Fig. 4 I). In addition to being part of the latter interaction hub, the triskelion-shaped FAP76 formed at least three more interfaces with neighboring structures: connections to each other in the longitudinal direction (Fig. 4 I) and two connections to the neighboring C1d projections (Fig. 4 J). The C1d projections themselves were bound every 32 nm to C1 protofilaments 4 and 6 (Fig. 4, G and H; Fig. 6, E and F; and Fig. 8). Given the motility defects observed in all C1a-e-c mutants, including *fap216* with its very small structural defect, these subunits are likely involved in the same signal transduction pathway that regulates ciliary motility. Their connectivity with neighboring structures may provide the structural basis for signal transmission.

The C1e-c subcomplex, likely with C1d, forms a signaling pathway regulating ciliary motility

Most previously identified CA protein mutations, including the C1a-e-c mutant *pf16*, result in paralyzed or twitching-only cilia (Dutcher et al., 1984; Smith and Lefebvre 1996; Rupp et al., 2001). The four other C1a-e-c supercomplex mutants identified here, *fap76-1*, *fap81*, *fap92*, and *fap216*, have slow swimming phenotypes. However, loss of FAP92 did not result in major motility or structural defects, likely because the major C1a components remained largely unaffected. In contrast, cells of the remaining three mutants, *fap76-1*, *fap81*, and *fap216*, frequently changed swim orientations, resulting in curving swimming paths (Fig. 3 B). A straight swimming orientation, or sharp turns, seen in *Chlamydomonas* cells, are coupled to synchronous or asynchronous ciliary beating, respectively (Polin et al., 2009). Consistent with this, the period of synchronous beating between the two flagella of the mutant cells was shorter than that of WT (Video 3), causing frequent reorientation during swimming. If the overall shape of the flagellar waveform is not changed, as is the case here (Video 3), then the loss of synchrony between the flagella could be caused by random delays in switching of dynein activity from one side of the axoneme to the other in one of the two flagella. Our findings indicate that the C1e-c subcomplex, which is largely composed of FAP76, FAP81, and FAP216, may play a critical role in coordinating the oscillatory switching of dynein activity, and thus in maintaining synchrony between the two beating cilia.

The C1e-c subcomplex may act in the same regulatory pathway as the adjacent C1d projection, because previous studies reported similar motility defects for *Chlamydomonas* C1d mutants, i.e., slow swimming, uncoordinated ciliary beating, and a deficient photoshock response (DiPetrillo and Smith, 2010, 2011; Brown et al., 2012). In our model, the C1e-c subcomplex is part of the protein network that requires PF16 for stable assembly, but it has a 32-nm periodicity, identical to that of the C1d projection and twice that of the C1a projection. Our cryo-ET data revealed that the C1c projection interacts directly with the C1d projection through FAP76 and FAP81 (Fig. 8 B), and our combined sucrose gradient and MS data provided evidence that the PF16-associated protein network is physically attached to at least two proteins previously assigned to C1d. Thus, the C1e-c subcomplex may be physically and functionally distinct from the C1a projection, but closely related to C1d. Given the more severe motility defects observed in the C1d mutants (DiPetrillo and Smith, 2010, 2011; Brown et al., 2012), regulatory signals might be transmitted from the C1d projection to the C1e-c subcomplex through their direct connections. From the C1e-c subcomplex, the signal could be sent downstream either to the C1a projection or to RS heads to ultimately modulate dynein activities. One such signal could be initiated by changes in intraflagellar calcium concentration, because the C1d protein FAP221 binds calmodulin in a Ca^{2+}-sensitive manner and thus could mediate Ca^{2+}-induced changes in flagellar waveform (Witman, 1993; DiPetrillo and Smith, 2010; Brown et al., 2012). Although FAP76 could still bind to the C1 microtubule and connect to the neighboring C1d projection in the *fap81* mutant (Fig. S5, A–F), the positional flexibility of FAP76 caused by loss of its N-terminal binding partner FAP81 could be sufficient to disrupt the proposed signal-transmission cascade between C1d and C1c-e.

Spatial association between the CA and the DMT-associated dynein regulators

How the CA signals are transmitted to DMT dyneins through the interaction with RSs is poorly understood. In *Chlamydomonas*, the CA is slightly twisted around its longitudinal axis (90° twist over 2-µm CA length; Carbajal-González et al., 2013), and the CA has been shown to rotate around the ciliary axis during motility (Kamiya, 1982). Therefore, the CA projections in *Chlamydomonas* flagella are not expected to have a fixed interaction with RSs from a specific DMT. However, previous in vitro microtubule sliding assays and classic thin-section EM showed that the C1 microtubule was predominantly oriented toward the set of actively sliding DMTs, which switches between DMTs 2–4 and 6–8 in the two halves of the axoneme (Wargo and Smith, 2003). In addition, the orientation of the C1 microtubule seems to be correlated with the flagellar bending direction, as observed in axonemes prepared by freeze-etching (Mitchell, 2003). Switching of ciliary bending direction, which is critical to generate the undulating motion typical for cilia, correlates with the switching of dynein activity that drives interdoublet sliding between either DMTs 2–4 or 6–8 (Wais-Steider and Satir, 1979; Tamm and Tamm, 1984; Sale, 1986; Hayashi and Shingyoji, 2008; Lin and Nicastro, 2018). Therefore, we examined the spatial association between the CA projections and DMTs in WT and mutant axonemes. We found that the C1a-e-c supercomplex predominantly faced DMTs 6–8 in isolated and inactive WT and

C1e-c mutant axonemes (Fig. S3 H). The preferential orientation of the C1a-e-c supercomplex toward DMTs 6–8 is consistent with the CA projections playing a role in controlling ciliary bending direction. However, the axonemes we isolated were inactive (no ATP added in the buffer); therefore, all dyneins were in their post–power stroke conformation. Future studies of the CA in actively beating cilia could reveal if the relative location of the C1a-e-c supercomplex switches between DMTs 2–4 and 6–8 in a bend direction–specific manner.

FAP216 plays a role in chemical signal transduction between CA and RSs

A previous study reported that the motility defects of the *pf6* mutant, which lacks most of the C1a-e projections (not depicted), could be restored by adding exogenous tags to the RS heads (Oda et al., 2014). This result led to a working model that the CP–RS communication is, at least in part, mediated by nonspecific collision-based mechano-signaling between the CA projections and RS heads without requiring specific physiological protein–protein interactions at the CP–RS interface (Oda et al., 2014). The severe motility defects of the *fap216* mutant suggest that a mechanically intact CA–RS interface alone is not sufficient for proper CA–RS communication and regulation of dynein activity. Despite missing only a small density in the center of the CA, 18 nm away from the interface with the RS heads (Figs. 7 G and 8), the motility defect in *fap216* is as severe as in *fap81*, which lacks the entire C1e-c subcomplex. This raises the possibility that FAP216 contributes to a chemical signal transduction pathway between the CA and RSs to regulate ciliary motility.

Conclusion

In humans, many axonemal gene mutations have been shown to cause ciliopathies such as PCD (Horani and Ferkol, 2018). Historically, conventional TEM analysis of patient ciliary samples is considered a standard clinical diagnostic tool for PCD (Kott et al., 2013; El Khouri et al., 2016; Edelbusch et al., 2017). However, the resolution of conventional TEM is greatly limited, hindering the diagnosis of PCD types caused by minor structural alterations. Therefore, future comparisons of normal and potential ciliopathy CA structures by cryo-ET may facilitate recognition of previously undiagnosed or misinterpreted defects in human patients (Lin et al., 2014). Overall, our study provides a partial "molecular blueprint" for the C1a-e-c supercomplex that will be the foundation for future studies into detailed protein–protein interactions and molecular mechanisms by which CA signals are transmitted to the RS heads to ultimately regulate dynein activity and thus ciliary beating.

Materials and methods

Strains and culture conditions

Chlamydomonas WT strains used were g1 (*nit1*, *agg1*, *mt+*, a cross of *nit1-305* to CC-124 [Pazour et al., 1995]; *Chlamydomonas* Resource Center, https://www.chlamycollection.org, CC-5415), and A54-e18 (CC-2929). The mutant *pf28* (CC-3661) was obtained from *Chlamydomonas* Resource Center, and *pf16A* and *pf16* (D2, the *pf16* insertional allele) were generated as previously described (Dutcher et al., 1984; Smith and Lefebvre, 1996). The *pf16* (D2) strain was used for MS and cryo-ET analyses. The *pf28* and *pf16* (D2) strains were mated to generate *pf28;pf16* double mutant (DiBella et al., 2004). Strains from the CLiP (Li et al., 2016) included the parental strain CC-5325 and the insertional mutants *fap76-1* (CLiP ID: LMJ.RY0402.089534), *fap76-2* (LMJ.RY0402.088713), *fap81* (LMJ.RY0402.092632), *fap92* (LMJ.RY0402.204383), and *fap216* (LMJ.RY0402.218389), all of which were obtained from the *Chlamydomonas* Resource Center. For MS analysis of axonemal proteins, *fap76-1* was crossed to g1 (Zhao et al., 2019), which served as the control. As previously described (Fu et al., 2018), *Chlamydomonas* cells were maintained in solid Tris-acetate-phosphate (TAP) plates (supplied with 7.5 µg/ml paromomycin for CLiP mutants) and cultured in liquid TAP medium or modified M medium (Witman, 1986) under a 12:12-h light:dark cycle at 23°C with filtered air bubbling into the growing culture. Insertion sites of CLiP mutants were confirmed by PCR (Fig. S2 A) using the primers indicated in Table S4.

Generation of tagged strains and rescue of mutants

To generate the BCCP-tagged *pf16;PF16::BCCP* strain, the BCCP domain of *Chlamydomonas* acetyl-coenzyme A carboxylase gene (Cre17.g715250, Phytozome 12; amino acids 141–228 were used for tagging) was amplified by RT-PCR from genomic DNA from WT *Chlamydomonas* (strain A54-e18, CC-2929) as previously described (Oda and Kikkawa, 2013). A BCCP-tagged *PF16* construct was generated by ligating the BCCP domain into the C-terminal MluI site of the pB6D2 plasmid that contains the *PF16* gene (a 4.5-kb genomic fragment in pBluescript that rescues the mutant phenotype, Smith and Lefebvre, 1996). The BCCP-pB6D2 plasmid was cotransformed into *pf16* (D2), along with the *APH-VIII* gene, using the glass bead method (Kindle, 1990). Transformed cells were plated onto TAP plates with 20 µg/ml paromomycin. Cells were screened first for rescued motility, then by Western blot of axonemes to confirm the presence of PF16 along with the BCCP tag (rabbit anti-PF16 antibodies; 1:1,000, affinity purified; Smith and Lefebvre, 1996) and a streptavidin-HRP probe (1:5,000, GE Healthcare, GERPN1231).

For the FAP76-BCCP rescue construct, sequence encoding the BCCP tag was amplified from pIC2L-BCCPC-3xHA-Hyg (kindly provided by Professor Toshiyuki Oda, University of Yamanashi, Kofu, Japan) with primers F7/R7 (Table S4) and then was inserted into the MauB1 site of the plasmid pBC8, which contains a hygromycin cassette and the complete *FAP76* gene (Cre09.g387689, Phytozome 12), to yield pBC25.

For the FAP216-BCCP rescue construct, portions of the *FAP216* gene (Cre12.g497200, Phytozome 12) were amplified from genomic DNA with primers F8/R8, F9/R9, and F10/R10 (Table S4). Plasmid pBH (Zhao et al., 2019) was linearized by digestion with NdeI and SbfI, and the *FAP216* fragments were assembled into it using NEBuilder HiFi DNA assembly master mix (NEB), yielding pBC26. To introduce the BCCP tag, the sequence encoding the tag was amplified from pIC2L-BCCPC-3xHA-Hyg with primers F11/R11 (Table S4) and then cloned into pBC26 at the MauB1 site, yielding pBC27.

All constructs were verified by sequencing. *Chlamydomonas* cells were transformed by the glass bead method (Kindle, 1990).

After transformation, cells were grown on TAP agar supplemented with 10 µg/ml hygromycin (Sigma-Aldrich). Cells were screened for rescued motility; incorporation of the construct was then confirmed by Western blotting with a streptavidin-HRP probe (1:3,000, Molecular Probes). West Dura Extended Duration Substrate (Thermo Fisher Scientific) was used for HRP detection.

RNA isolation and RT-PCR

Total RNA was isolated from WT and *fap92* cells using RNeasy Plus Mini Kit (Qiagen). cDNA synthesis was performed using SuperScript IV reverse transcription (Invitrogen) following the manufacturer's protocol, and both Oligo(dT)$_{20}$ and random hexamers were used as primers. *FAP92* (Cre13.g562250, Phytozome 12) fragments were then amplified using primers F12/R12 (Table S4) and sequenced. The gene encoding G protein β subunit (Cre06.g278222, Phytozome 12; Schloss, 1990) was used as the control and amplified with primers F13/R13 (Table S4).

Sucrose gradient analysis

Isolated axonemes were extracted in 0.5 M KI in NaLow (10 mM Hepes, pH 7.5, 5 mM $MgSO_4$, 1 mM DTT, 0.5 mM EDTA, and 30 mM NaCl) at 6 mg/ml for 30 min on ice. After centrifugation, the extracted proteins were dialyzed into NaLow and then loaded onto a 5–20% sucrose gradient made in NaLow and centrifuged at 35,000 rpm for 16 h in a SW41Ti rotor (Beckman Coulter). Gradients were fractionated (0.5 ml fractions) from bottom (fraction 1) to top (fraction 24).

For Western blot analyses, the sucrose gradient fractions were separated using SDS-PAGE and transferred to polyvinylidene difluoride membrane. For detection of PF16 protein, membranes were probed with anti-PF16 antibodies (1:1,000, affinity purified). The ECL Prime Kit (GE Healthcare) was used for HRP detection.

Immunofluorescence microscopy of *fap76-1* and *fap76-1;BCCP::FAP76*

Immunofluorescence microscopy was performed as described previously (Zhao et al., 2019). Briefly, the slides with attached intact axonemes were treated overnight at 4°C with blocking buffer containing the diluted primary antibody (mouse anti-acetylated tubulin, Sigma-Aldrich, clone 6-11B-1, 1:1,000). On the next day, the slides were washed four times over 1 h with blocking buffer, and then treated for 1 h with blocking buffer containing the secondary antibody (F(ab')2-goat anti-mouse IgG (H+L) cross-adsorbed secondary antibody, Alexa Fluor 568, Invitrogen, A11019, 1:1,000) and Streptavidin (Alexa Fluor 488, Invitrogen, A32354, 1:200). The samples were mounted and examined as before (Zhao et al., 2019) using structured illumination microscopy performed on a DeltaVision OMX system (GE Healthcare) with a 1.42 NA 60× Plan-Apochromat objective lens (Olympus) and immersion oil with a refraction index of 1.512. Structured illumination microscopy images were reconstructed with softWoRx 6.1.3 (GE Healthcare). Capture times and adjustments were the same for images with the same antibody. Image brightness and contrast were adjusted using ImageJ (National Institutes of Health).

Analysis of motility phenotypes

All observations and recordings except for high-speed video were performed on cells grown in liquid M medium at room temperature. The swimming speed and swimming paths of cells were analyzed as described previously (Zhao et al., 2019). To analyze swimming speed, 50 µl of cell culture were transferred to a plastic chamber (0.127-mm-deep Fisherbrand UriSystem DeciSlide; Thermo Fisher Scientific). Cells were imaged with nonactinic (deep-red) light using a Zeiss inverted microscope equipped with a 16×/0.35 NA Plan objective and a Kopp #2408 red long-pass filter (Kopp Glass). Movies were recorded at 30 images/s with a digital charge-coupled device (CCD) camera (UP-610; UNIQ Vision) and Video Savant 3.0 software (IO Industries). Swimming speeds were determined using ImageJ as previously described (Awata et al., 2015). To record swimming paths, 1-s exposures were acquired using white light and phase-contrast optics on a Zeiss Axioskop 2 Plus microscope equipped with a 20× Plan-NeoFluar 0.5 NA Ph2 objective, a digital CCD camera (AxioCam MRm), and AxioVision 3.1 software (Zeiss).

For high-speed video recording of swimming cells, a PCO 1200HS camera with Camware software (Cooke Corp.) was used (500 frames/s) on an Axioskop microscope (Zeiss), and videos were taken with a 40×/0.65 NA objective lens under phase-contrast mode. Cells were in TAP medium at room temperature. A red filter placed on the light source was removed to induce waveform switching due to photoshock. Videos (saved at 20 frames/s) were created in ImageJ (Schneider et al., 2012), and the videos of different swimming cells were combined in Photoshop to generate Video 3. To evaluate photoshock ability, at least 30 cells were analyzed.

Axoneme preparation

Axonemes of *Chlamydomonas* cells were purified by the pH shock method as previously described (Witman, 1986; Song et al., 2015). Briefly, cells were cultured in liquid TAP medium, collected by centrifugation (2,200 rpm for 5 min), and washed twice with fresh M-N/5 minimal medium (Iomini et al., 2009). The cell pellet was resuspended in pH shock buffer (10 mM Hepes, 1 mM $SrCl_2$, 4% sucrose, and 1 mM DTT, pH 7.4), and 0.5 M acetic acid was added to the buffer to reduce the pH to 4.3. After 80 s, 1 M KOH was added to increase the pH to 7.2; the pH shock treatment was performed on ice. After pH shock, 5 mM $MgSO_4$, 1 mM EGTA, 0.1 mM EDTA, and 100 µl protease inhibitor (Sigma-Aldrich) were added to the solution. The solution was centrifuged (1800 *g* for 10 min, 4°C) to separate the detached flagella from the cell bodies. To further purify the flagella, the flagella-containing supernatant was centrifuged twice with a 20% sucrose cushion (2,400 *g* for 10 min, 4°C). After centrifugation, 1% IGEPAL CA-630 (Sigma-Aldrich) was added to the supernatant to demembranate the flagella for 20 min at 4°C. Axonemes were collected by centrifugation (10,000 *g* for 10 min, 4°C), and the freshly isolated axonemes were resuspended in HMEEK buffer (30 mM Hepes, 25 mM KCl, 5 mM $MgSO_4$, 0.1 mM EDTA, and 1 mM EGTA, pH 7.2). Axonemal samples were either plunge-frozen for cryo-ET or stored at −80°C for biochemical assays.

Streptavidin gold labeling

For gold labeling of axonemes from *pf16;PF16::BCCP* and *fap76-1;BCCP::FAP76*, 5 µl of 80 µg/ml 1.4-nm-sized streptavidin nanogold particles (Nanoprobes) was added to 200 µl of the freshly prepared axonemal solution and incubated for 4 h at 4°C. Meanwhile, 200 µl of samples without added streptavidin gold particles were also prepared as control. The axonemes were washed by adding 800 µl HMEEK, collected by centrifugation (10,000 *g* for 1 min, 4°C), and resuspended in HMEEK. Axonemal samples treated with and without streptavidin gold were plunge-frozen for cryo-ET analysis. In addition, 40 µg of the axonemes from the *fap76-1;BCCP::FAP76* sample (with and without gold particles) were separated on a 4–12% gradient SDS-polyacrylamide gel. The gel was stained with a silver enhancement kit (Nanoprobes) for 45 min at room temperature, and the bands were imaged using a ChemiDoc Touch Imaging System (Bio-Rad). The gel was stained with Coomassie brilliant blue for 2 h and destained until the background was clear.

Liquid chromatography–MS/MS

Axonemal protein (40 µg) of the WT, *fap76-2*, *fap81*, and *fap216* strains were separated on a 4–12% gradient SDS-polyacrylamide gel. After the proteins had entered the gel 3.0–3.5 cm, the gel was stained with Coomassie brilliant blue for 30 min and destained until the background was clear. Each gel lane was cut into four slices, and each slice was further excised into 1-mm cubic pieces. In-gel trypsin digestion and peptide identification were conducted by the proteomics core facility at the University of Texas Southwestern Medical Center. Proteins that had >10 unique peptides identified in the WT sample were selected for further analyses. Quantification of the mutant/WT ratio for each axonemal protein was estimated by the MIC sin (matched isotope pattern chromatogram spectral index) value (Trudgian et al., 2011). Data for *pf16* are from Zhao et al., (2019) (repeat 2, Table S4). Some data for *fap76-1* are from Zhao et al. (2019) (repeat 2, Table S6). Intensity-based absolute quantification (IBAQ; Schwanhäusser et al., 2011) and Top3 precursor quantification methods (Top3; Silva et al., 2006) were used to estimate the abundance of each protein.

For MS studies of sucrose gradient fractions from *pf16*(D2) or *pf28;pf16*(D2) axonemal extracts, proteins were run 0.5 cm into a 10% polyacrylamide resolving gel and stained with Coomassie brilliant blue. The protein-containing segments were excised and analyzed at the University of Massachusetts Medical School by matrix-assisted laser desorption/ionization time-of-flight tandem MS with postsource decay.

Cryo-ET

Freshly prepared axonemal samples (30 µl) were gently mixed with 10 µl of 10-fold-concentrated, BSA-coated 10-nm gold solution (Iancu et al., 2006). 4 µl of the solution was applied to a glow-discharged (30 s at −35 mA) copper R2/2 holey carbon grid (Quantifoil Micro Tools). After removing excess liquid by blotting the grid from the back side with Whatman filter paper no. 1 for 2 s, the grid was plunge-frozen into liquid ethane using a homemade plunge-freezer. Grids were then stored in liquid nitrogen until use.

For most strains, grids were mounted in Autogrids (Thermo Fisher Scientific) and loaded into a Titan Krios transmission electron microscope (Thermo Fisher Scientific) operated at 300 kV. The microscope control software SerialEM (Mastronarde, 2005) was used to acquire tilt series images in low-dose mode from −60° to 60° with 1.5°–2.5° increments using a dose-symmetric tilting scheme (Hagen et al., 2017). The images were recorded with a 4,000 × 4,000 K2 direct electron detection camera (Gatan) in counting mode (15 frames, 0.4-s exposure time per frame, dose rate of 8 electrons/pixel/s for each tilt image). The postcolumn energy filter (Gatan) was operated in zero-loss mode (20-eV slit width), and a Volta-Phase-Plate (Danev et al., 2014) was used with −0.5-µm defocus. The magnification was set to 26,000 with an effective pixel size of 5.5 Å. The total electron dose per tilt series was limited to ∼100 e/Å^2.

Grids of the *pf16* and *pf16;PF16::BCCP* samples were imaged using a Tecnai F30 transmission electron microscope (Thermo Fisher Scientific) operated at 300 kV. A 2,000 × 2,000 CCD camera (Gatan) was used for recording tilt series images with SerialEM (Mastronarde, 2005) as described above, except neither dose-symmetric tilting nor Volta-Phase-Plate were used, and the defocus was set to −8 µm. The magnification was 13,500, with an effective pixel size of 1.077 nm.

Image processing

Frame alignment for data collected on the K2 camera, alignment of tilt serial images, and tomogram reconstruction were performed as previously described (Fu et al., 2018). In brief, motion correction of the frames was done with a script extracted from IMOD software (Kremer et al., 1996). IMOD software was also used for aligning the tilt serial images using the 10-nm gold particles as fiducial markers and for reconstructing the tomograms by weighted back-projection. For subtomogram averaging, either CA or DMT repeats were picked from the raw tomograms, and alignment and missing-wedge compensated averaging were performed using PEET software (Nicastro et al., 2006), which is integrated in the IMOD software package. The axoneme and CA orientation (proximal to distal) was determined for each tomogram based on both DMT orientation in the axoneme cross section (e.g., "clockwise" orientation as shown in Fig. 1 H represents "viewed from distal") and initial averages that included only the CA repeats within each tomogram. After the CA polarity and the same center of the repeat were determined for each tomogram, a second alignment was performed combining the CA repeats from all tomograms in the correct orientation and periodicity register. After global alignment of all CA repeats, the alignment of each individual CA microtubule was refined by local alignment of each microtubule and its associated projections separately, while the other microtubule was masked as described previously (Carbajal-González et al., 2013). Visualization of the 3D structures of the averaged CA and DMT repeats was done with the UCSF Chimera package software (Pettersen et al., 2004). For generating the isosurface rendering images, the same isosurface threshold was applied to the WT and mutant averages. Classification analyses used a principal component analysis clustering method incorporated in the PEET software (Heumann et al., 2011). The number of tomograms and

CA repeats, as well as the estimated resolution of the averages (using FSC 0.5 criterion), are summarized for each strain in Table S3.

Data access

The 3D averaged structures of the CA from different strains have been deposited in the Electron Microscopy Data Bank under accession codes EMD-20160 (WT), EMD-20161 (*fap92*), EMD-20162 (*fap76-1*), EMD-20163 (*fap76-2*), EMD-20164 (*fap81*), EMD-20165 (*fap216*), and EMD-20166 (*fap76-1;fap81*).

Online supplemental material

Fig. S1 shows different conformational states of the C2a projection and refined structural details within the C1a-e-c supercomplex. Fig. S2 shows the genotyping analysis by PCR of the *fap76-1*, *fap76-2*, *fap81*, *fap92*, and *fap216* CLiP mutants to confirm disruption of the corresponding genes; and immunoblot analysis of PF16 in *pf16* rescue strain and seven of the strains studied. Fig. S3 shows the isosurface renderings of averaged 96-nm axonemal DMT repeats from WT and the CLiP mutants, confirming that the mutants have no DMT-associated defects; the orientation of the C1a-e-c supercomplex relative to specific DMTs is also shown. Fig. S4 depicts insertion sites for the *fap76* mutant alleles and shows the phenotype analyses and structural defects of the *fap76-2* mutant. Fig. S5 provides classification analyses of the *fap81* and *fap216* mutant showing that half of the *fap81* CA particles contain FAP76 density, and that the C1e density was reduced in the *fap216* mutant. Table S1 lists all the proteins that cosedimented with PF16 in our sucrose gradient analysis and that were significantly reduced in *pf28;pf16* axonemes as revealed by sucrose gradient and MS analyses. Table S2 provides unique peptide numbers and mutant/WT ratios of additional C1 proteins identified by Zhao et al. (2019), but not by our sucrose gradient analyses. Table S3 summarizes the image processing information (number of tomograms, CA particles, and resolution) for the strains used in this study. Table S4 lists the primers used in this study. Video 1 shows the 3D isosurface rendering of the averaged *Chlamydomonas* WT CA repeat. Video 2 summarizes the location and structural organization for FAP76, FAP81, FAP92, and FAP216 within the ciliary CA structure. Video 3 is a combination of videos showing swimming cells of *Chlamydomonas* WT and the mutant strains studied here.

Acknowledgments

We thank T. Loreng of Dartmouth College for technical assistance and K. Cai and L. Gui of University of Texas Southwestern Medical Center (UTSW) for discussions and critical reading of the manuscript. We thank A. Lemoff and the proteomics core facility at UTSW and M. Dubuke of the MS facility at the University of Massachusetts Medical School for the liquid chromatography-MS/MS analyses.

We are grateful to D. Stoddard for management of the UTSW cryo-electron microscope facility, which is funded in part by a Cancer Prevention and Research Institute of Texas Core Facility Award (RP170644). This study was supported by National Institutes of Health grants R01 GM083122 to D. Nicastro, R35 GM122574 to G.B. Witman, and R01 GM112050 to E.F. Smith, and by Cancer Prevention and Research Institute of Texas grant RR140082 to D. Nicastro.

The authors declare no competing financial interests.

Author contributions: G. Fu and D. Nicastro conceived the study and designed experiments. G. Fu, K. Song, and Z. Shang performed cryo-ET data collection and analysis. L. Zhao, E. Dymek, and Y. Hou analyzed the phenotypes of mutants and generated rescued strains. G. Fu and L. Zhao analyzed the liquid chromatography-MS/MS data. E. Dymek and L. Zhao performed sucrose gradient and Western blot analyses. N. Phan and L. Zhao performed genotyping analysis of the CLiP mutants. G. Fu and D. Nicastro wrote the manuscript, and G. Fu, D. Nicastro, L. Zhao, G.B. Witman, and E.F. Smith edited the manuscript.

Submitted: 3 June 2019
Revised: 13 September 2019
Accepted: 23 September 2019

References

Afzelius, B.A. 2004. Cilia-related diseases. *J. Pathol.* 204:470–477. https://doi.org/10.1002/path.1652

Awata, J., K. Song, J. Lin, S.M. King, M.J. Sanderson, D. Nicastro, and G.B. Witman. 2015. DRC3 connects the N-DRC to dynein g to regulate flagellar waveform. *Mol. Biol. Cell.* 26:2788–2800. https://doi.org/10.1091/mbc.E15-01-0018

Bower, R., K. VanderWaal, E. O'Toole, L. Fox, C. Perrone, J. Mueller, M. Wirschell, R. Kamiya, W.S. Sale, and M.E. Porter. 2009. IC138 defines a subdomain at the base of the I1 dynein that regulates microtubule sliding and flagellar motility. *Mol. Biol. Cell.* 20:3055–3063. https://doi.org/10.1091/mbc.e09-04-0277

Brilot, A.F., J.Z. Chen, A. Cheng, J. Pan, S.C. Harrison, C.S. Potter, B. Carragher, R. Henderson, and N. Grigorieff. 2012. Beam-induced motion of vitrified specimen on holey carbon film. *J. Struct. Biol.* 177:630–637. https://doi.org/10.1016/j.jsb.2012.02.003

Brown, J.M., C.G. Dipetrillo, E.F. Smith, and G.B. Witman. 2012. A FAP46 mutant provides new insights into the function and assembly of the C1d complex of the ciliary central apparatus. *J. Cell Sci.* 125:3904–3913. https://doi.org/10.1242/jcs.107151

Carbajal-González, B.I., T. Heuser, X. Fu, J. Lin, B.W. Smith, D.R. Mitchell, and D. Nicastro. 2013. Conserved structural motifs in the central pair complex of eukaryotic flagella. *Cytoskeleton (Hoboken).* 70:101–120. https://doi.org/10.1002/cm.21094

Cheng, Y., N. Grigorieff, P.A. Penczek, and T. Walz. 2015. A primer to single-particle cryo-electron microscopy. *Cell.* 161:438–449. https://doi.org/10.1016/j.cell.2015.03.050

Danev, R., B. Buijsse, M. Khoshouei, J.M. Plitzko, and W. Baumeister. 2014. Volta potential phase plate for in-focus phase contrast transmission electron microscopy. *Proc. Natl. Acad. Sci. USA.* 111:15635–15640. https://doi.org/10.1073/pnas.1418377111

DiBella, L.M., E.F. Smith, R.S. Patel-King, K. Wakabayashi, and S.M. King. 2004. A novel Tctex2-related light chain is required for stability of inner dynein arm I1 and motor function in the *Chlamydomonas* flagellum. *J. Biol. Chem.* 279:21666–21676. https://doi.org/10.1074/jbc.M313540200

DiPetrillo, C.G., and E.F. Smith. 2010. Pcdp1 is a central apparatus protein that binds Ca(2+)-calmodulin and regulates ciliary motility. *J. Cell Biol.* 189:601–612. https://doi.org/10.1083/jcb.200912009

DiPetrillo, C.G., and E.F. Smith. 2011. The Pcdp1 complex coordinates the activity of dynein isoforms to produce wild-type ciliary motility. *Mol. Biol. Cell.* 22:4527–4538. https://doi.org/10.1091/mbc.e11-08-0739

Dutcher, S.K., B. Huang, and D.J. Luck. 1984. Genetic dissection of the central pair microtubules of the flagella of *Chlamydomonas* reinhardtii. *J. Cell Biol.* 98:229–236. https://doi.org/10.1083/jcb.98.1.229

Dymek, E.E., and E.F. Smith. 2007. A conserved CaM- and radial spoke associated complex mediates regulation of flagellar dynein activity. *J. Cell Biol.* 179:515–526. https://doi.org/10.1083/jcb.200703107

Edelbusch, C., S. Cindrić, G.W. Dougherty, N.T. Loges, H. Olbrich, J. Rivlin, J. Wallmeier, P. Pennekamp, I. Amirav, and H. Omran. 2017. Mutation of serine/threonine protein kinase 36 (STK36) causes primary ciliary dyskinesia with a central pair defect. *Hum. Mutat.* 38:964–969. https://doi.org/10.1002/humu.23261

El Khouri, E., L. Thomas, L. Jeanson, E. Bequignon, B. Vallette, P. Duquesnoy, G. Montantin, B. Copin, F.D.-L. Moal, S. Blanchon, et al. 2016. Mutations in DNAJB13, encoding an HSP40 family member, cause primary ciliary dyskinesia and male infertility. *Am. J. Hum. Genet.* 99:489–500. https://doi.org/10.1016/j.ajhg.2016.06.022

Fliegauf, M., T. Benzing, and H. Omran. 2007. When cilia go bad: cilia defects and ciliopathies. *Nat. Rev. Mol. Cell Biol.* 8:880–893. https://doi.org/10.1038/nrm2278

Fu, G., Q. Wang, N. Phan, P. Urbanska, E. Joachimiak, J. Lin, D. Wloga, and D. Nicastro. 2018. The I1 dynein-associated tether and tether head complex is a conserved regulator of ciliary motility. *Mol. Biol. Cell.* 29:1048–1059. https://doi.org/10.1091/mbc.E18-02-0142

Hagen, W.J.H., W. Wan, and J.A.G. Briggs. 2017. Implementation of a cryo-electron tomography tilt-scheme optimized for high resolution subtomogram averaging. *J. Struct. Biol.* 197:191–198. https://doi.org/10.1016/j.jsb.2016.06.007

Hayashi, S., and C. Shingyoji. 2008. Mechanism of flagellar oscillation-bending-induced switching of dynein activity in elastase-treated axonemes of sea urchin sperm. *J. Cell Sci.* 121:2833–2843. https://doi.org/10.1242/jcs.031195

Heumann, J.M., A. Hoenger, and D.N. Mastronarde. 2011. Clustering and variance maps for cryo-electron tomography using wedge-masked differences. *J. Struct. Biol.* 175:288–299. https://doi.org/10.1016/j.jsb.2011.05.011

Heuser, T., C.F. Barber, J. Lin, J. Krell, M. Rebesco, M.E. Porter, and D. Nicastro. 2012a. Cryoelectron tomography reveals doublet-specific structures and unique interactions in the I1 dynein. *Proc. Natl. Acad. Sci. USA.* 109:E2067–E2076. https://doi.org/10.1073/pnas.1120690109

Heuser, T., E.E. Dymek, J. Lin, E.F. Smith, and D. Nicastro. 2012b. The CSC connects three major axonemal complexes involved in dynein regulation. *Mol. Biol. Cell.* 23:3143–3155. https://doi.org/10.1091/mbc.e12-05-0357

Heuser, T., M. Raytchev, J. Krell, M.E. Porter, and D. Nicastro. 2009. The dynein regulatory complex is the nexin link and a major regulatory node in cilia and flagella. *J. Cell Biol.* 187:921–933. https://doi.org/10.1083/jcb.200908067

Horani, A., and T.W. Ferkol. 2018. Advances in the genetics of primary ciliary dyskinesia: clinical implications. *Chest.* 154:645–652. https://doi.org/10.1016/j.chest.2018.05.007

Iancu, C.V., W.F. Tivol, J.B. Schooler, D.P. Dias, G.P. Henderson, G.E. Murphy, E.R. Wright, Z. Li, Z. Yu, A. Briegel, et al. 2006. Electron cryotomography sample preparation using the Vitrobot. *Nat. Protoc.* 1:2813–2819. https://doi.org/10.1038/nprot.2006.432

Iomini, C., J.E. Till, and S.K. Dutcher. 2009. Genetic and phenotypic analysis of flagellar assembly mutants in *Chlamydomonas* reinhardtii. *Methods Cell Biol.* 93:121–143. https://doi.org/10.1016/S0091-679X(08)93007-7

Kamiya, R. 1982. Extrusion and Rotation of the central-pair microtubules in detergent-treated *Chlamydomonas* flagella. *Prog. Clin. Biol. Res.* 80:169–173. https://doi.org/10.1016/b978-0-12-615080-3.50025-2

Kamiya, R. 1988. Mutations at twelve independent loci result in absence of outer dynein arms in Chylamydomonas reinhardtii. *J. Cell Biol.* 107:2253–2258. https://doi.org/10.1083/jcb.107.6.2253

Kindle, K.L. 1990. High-frequency nuclear transformation of *Chlamydomonas reinhardtii*. *Proc. Natl. Acad. Sci. USA.* 87:1228–1232. https://doi.org/10.1073/pnas.87.3.1228

Kott, E., M. Legendre, B. Copin, J.-F. Papon, F. Dastot-Le Moal, G. Montantin, P. Duquesnoy, W. Piterboth, D. Amram, L. Bassinet, et al. 2013. Loss-of-function mutations in RSPH1 cause primary ciliary dyskinesia with central-complex and radial-spoke defects. *Am. J. Hum. Genet.* 93:561–570. https://doi.org/10.1016/j.ajhg.2013.07.013

Kremer, J.R., D.N. Mastronarde, and J.R. McIntosh. 1996. Computer visualization of three-dimensional image data using IMOD. *J. Struct. Biol.* 116:71–76. https://doi.org/10.1006/jsbi.1996.0013

Kubo, T., Y. Hou, D.A. Cochran, G.B. Witman, and T. Oda. 2018. A microtubule-dynein tethering complex regulates the axonemal inner dynein f (I1). *Mol. Biol. Cell.* 29:1060–1074. https://doi.org/10.1091/mbc.E17-11-0689

Lechtreck, K.-F., P. Delmotte, M.L. Robinson, M.J. Sanderson, and G.B. Witman. 2008. Mutations in Hydin impair ciliary motility in mice. *J. Cell Biol.* 180:633–643. https://doi.org/10.1083/jcb.200710162

Lee, L., D.R. Campagna, J.L. Pinkus, H. Mulhern, T.A. Wyatt, J.H. Sisson, J.A. Pavlik, G.S. Pinkus, and M.D. Fleming. 2008. Primary ciliary dyskinesia in mice lacking the novel ciliary protein Pcdp1. *Mol. Cell. Biol.* 28:949–957. https://doi.org/10.1128/MCB.00354-07

Li, X., R. Zhang, W. Patena, S.S. Gang, S.R. Blum, N. Ivanova, R. Yue, J.M. Robertson, P.A. Lefebvre, S.T. Fitz-Gibbon, et al. 2016. An indexed, mapped mutant library enables reverse genetics studies of biological processes in *Chlamydomonas reinhardtii*. *Plant Cell.* 28:367–387. https://doi.org/10.1105/tpc.15.00465

Lin, J., and D. Nicastro. 2018. Asymmetric distribution and spatial switching of dynein activity generates ciliary motility. *Science.* 360:eaar1968. https://doi.org/10.1126/science.aar1968

Lin, J., T.V. Le, K. Augspurger, D. Tritschler, R. Bower, G. Fu., C. Perrone, E.T. O'Toole, K.V. Mills, E. Dymek, et al. 2019. FAP57/WDR65 targets assembly of a subset of inner arm dyneins and connects to regulatory hubs in cilia. *Mol. Biol. Cell.* https://doi.org/10.1091/mbc.E19-07-0367

Lin, J., W. Yin, M.C. Smith, K. Song, M.W. Leigh, M.A. Zariwala, M.R. Knowles, L.E. Ostrowski, and D. Nicastro. 2014. Cryo-electron tomography reveals ciliary defects underlying human RSPH1 primary ciliary dyskinesia. *Nat. Commun.* 5:5727. https://doi.org/10.1038/ncomms6727

Loreng, T.D., and E.F. Smith. 2017. The central apparatus of cilia and eukaryotic flagella. *Cold Spring Harb. Perspect. Biol.* 9:a028118. https://doi.org/10.1101/cshperspect.a028118

Mastronarde, D.N. 2005. Automated electron microscope tomography using robust prediction of specimen movements. *J. Struct. Biol.* 152:36–51. https://doi.org/10.1016/j.jsb.2005.07.007

McKenzie, C.W., B. Craige, T.V. Kroeger, R. Finn, T.A. Wyatt, J.H. Sisson, J.A. Pavlik, L. Strittmatter, G.M. Hendricks, G.B. Witman, and L. Lee. 2015. CFAP54 is required for proper ciliary motility and assembly of the central pair apparatus in mice. *Mol. Biol. Cell.* 26:3140–3149. https://doi.org/10.1091/mbc.e15-02-0121

Mitchell, D.R. 2003. Reconstruction of the projection periodicity and surface architecture of the flagellar central pair complex. *Cell Motil. Cytoskeleton.* 55:188–199. https://doi.org/10.1002/cm.10121

Mitchell, D.R. 2004. Speculations on the evolution of 9+2 organelles and the role of central pair microtubules. *Biol. Cell.* 96:691–696. https://doi.org/10.1016/j.biolcel.2004.07.004

Mitchell, D.R., and J.L. Rosenbaum. 1985. A motile *Chlamydomonas* flagellar mutant that lacks outer dynein arms. *J. Cell Biol.* 100:1228–1234. https://doi.org/10.1083/jcb.100.4.1228

Mitchell, D.R., and W.S. Sale. 1999. Characterization of a *Chlamydomonas* insertional mutant that disrupts flagellar central pair microtubule-associated structures. *J. Cell Biol.* 144:293–304. https://doi.org/10.1083/jcb.144.2.293

Mitchell, D.R., and B. Smith. 2009. Analysis of the central pair microtubule complex in *Chlamydomonas reinhardtii*. *Methods Cell Biol.* 92:197–213. https://doi.org/10.1016/S0091-679X(08)92013-6

Nicastro, D., C. Schwartz, J. Pierson, R. Gaudette, M.E. Porter, and J.R. McIntosh. 2006. The molecular architecture of axonemes revealed by cryoelectron tomography. *Science.* 313:944–948. https://doi.org/10.1126/science.1128618

Oda, T., and M. Kikkawa. 2013. Novel structural labeling method using cryo-electron tomography and biotin-streptavidin system. *J. Struct. Biol.* 183:305–311. https://doi.org/10.1016/j.jsb.2013.07.003

Oda, T., H. Yanagisawa, T. Yagi, and M. Kikkawa. 2014. Mechanosignaling between central apparatus and radial spokes controls axonemal dynein activity. *J. Cell Biol.* 204:807–819. https://doi.org/10.1083/jcb.201312014

Pazour, G.J., N. Agrin, J. Leszyk, and G.B. Witman. 2005. Proteomic analysis of a eukaryotic cilium. *J. Cell Biol.* 170:103–113. https://doi.org/10.1083/jcb.200504008

Pazour, G.J., O.A. Sineshchekov, and G.B. Witman. 1995. Mutational analysis of the phototransduction pathway of *Chlamydomonas reinhardtii*. *J. Cell Biol.* 131:427–440. https://doi.org/10.1083/jcb.131.2.427

Pettersen, E.F., T.D. Goddard, C.C. Huang, G.S. Couch, D.M. Greenblatt, E.C. Meng, and T.E. Ferrin. 2004. UCSF Chimera--a visualization system for exploratory research and analysis. *J. Comput. Chem.* 25:1605–1612. https://doi.org/10.1002/jcc.20084

Piperno, G., K. Mead, M. LeDizet, and A. Moscatelli. 1994. Mutations in the "dynein regulatory complex" alter the ATP-insensitive binding sites for inner arm dyneins in *Chlamydomonas* axonemes. *J. Cell Biol.* 125:1109–1117. https://doi.org/10.1083/jcb.125.5.1109

Polin, M., I. Tuval, K. Drescher, J.P. Gollub, and R.E. Goldstein. 2009. *Chlamydomonas* swims with two "gears" in a eukaryotic version of run-and-tumble locomotion. *Science.* 325:487–490. https://doi.org/10.1126/science.1172667

Porter, M.E., and W.S. Sale. 2000. The 9 + 2 axoneme anchors multiple inner arm dyneins and a network of kinases and phosphatases that control motility. *J. Cell Biol.* 151:F37–F42. https://doi.org/10.1083/jcb.151.5.F37

Rupp, G., E. O'Toole, and M.E. Porter. 2001. The *Chlamydomonas* PF6 locus encodes a large alanine/proline-rich polypeptide that is required for assembly of a central pair projection and regulates flagellar motility. *Mol. Biol. Cell.* 12:739–751. https://doi.org/10.1091/mbc.12.3.739

Sale, W.S. 1986. The axonemal axis and Ca2+-induced asymmetry of active microtubule sliding in sea urchin sperm tails. *J. Cell Biol.* 102: 2042–2052. https://doi.org/10.1083/jcb.102.6.2042

Sale, W.S., and P. Satir. 1977. Direction of active sliding of microtubules in *Tetrahymena* cilia. *Proc. Natl. Acad. Sci. USA.* 74:2045–2049. https://doi.org/10.1073/pnas.74.5.2045

Schloss, J.A. 1990. A *Chlamydomonas* gene encodes a G protein β subunit-like polypeptide. *Mol. Gen. Genet.* 221:443–452. https://doi.org/10.1007/BF00259410

Schneider, C.A., W.S. Rasband, and K.W. Eliceiri. 2012. NIH Image to ImageJ: 25 years of image analysis. *Nat. Methods.* 9:671–675. https://doi.org/10.1038/nmeth.2089

Schwanhäusser, B., D. Busse, N. Li, G. Dittmar, J. Schuchhardt, J. Wolf, W. Chen, and M. Selbach. 2011. Global quantification of mammalian gene expression control. *Nature.* 473:337–342. https://doi.org/10.1038/nature10098

Silva, J.C., M.V. Gorenstein, G.Z. Li, J.P. Vissers, and S.J. Geromanos. 2006. Absolute quantification of proteins by LCMSE: a virtue of parallel MS acquisition. *Mol. Cell. Proteomics.* 5:144–156. https://doi.org/10.1074/mcp.M500230-MCP200

Smith, E.F. 2002. Regulation of flagellar dynein by the axonemal central apparatus. *Cell Motil. Cytoskeleton.* 52:33–42. https://doi.org/10.1002/cm.10031

Smith, E.F., and P.A. Lefebvre. 1996. PF16 encodes a protein with armadillo repeats and localizes to a single microtubule of the central apparatus in *Chlamydomonas* flagella. *J. Cell Biol.* 132:359–370. https://doi.org/10.1083/jcb.132.3.359

Smith, E.F., and P.A. Lefebvre. 1997a. The role of central apparatus components in flagellar motility and microtubule assembly. *Cell Motil. Cytoskeleton.* 38:1–8. https://doi.org/10.1002/(SICI)1097-0169(1997)38:1<1::AID-CM1>3.0.CO;2-C

Smith, E.F., and P.A. Lefebvre. 1997b. PF20 gene product contains WD repeats and localizes to the intermicrotubule bridges in *Chlamydomonas* flagella. *Mol. Biol. Cell.* 8:455–467. https://doi.org/10.1091/mbc.8.3.455

Smith, E.F., and W.S. Sale. 1992. Regulation of dynein-driven microtubule sliding by the radial spokes in flagella. *Science.* 257:1557–1559. https://doi.org/10.1126/science.1387971

Smith, E.F., and P. Yang. 2004. The radial spokes and central apparatus: mechano-chemical transducers that regulate flagellar motility. *Cell Motil. Cytoskeleton.* 57:8–17. https://doi.org/10.1002/cm.10155

Song, K., J. Awata, D. Tritschler, R. Bower, G.B. Witman, M.E. Porter, and D. Nicastro. 2015. In situ localization of N and C termini of subunits of the flagellar nexin-dynein regulatory complex (N-DRC) using SNAP tag and cryo-electron tomography. *J. Biol. Chem.* 290:5341–5353. https://doi.org/10.1074/jbc.M114.626556

Summers, K.E., and I.R. Gibbons. 1971. Adenosine triphosphate-induced sliding of tubules in trypsin-treated flagella of sea-urchin sperm. *Proc. Natl. Acad. Sci. USA.* 68:3092–3096. https://doi.org/10.1073/pnas.68.12.3092

Tamm, S.L., and S. Tamm. 1984. Alternate patterns of doublet microtubule sliding in ATP-disintegrated macrocilia of the ctenophore Beroë. *J. Cell Biol.* 99:1364–1371. https://doi.org/10.1083/jcb.99.4.1364

Teves, M.E., D.R. Nagarkatti-Gude, Z. Zhang, and J.F. Strauss III. 2016. Mammalian axoneme central pair complex proteins: Broader roles revealed by gene knockout phenotypes. *Cytoskeleton (Hoboken).* 73:3–22. https://doi.org/10.1002/cm.21271

Trudgian, D.C., G. Ridlova, R. Fischer, M.M. Mackeen, N. Ternette, O. Acuto, B.M. Kessler, and B. Thomas. 2011. Comparative evaluation of label-free SINQ normalized spectral index quantitation in the central proteomics facilities pipeline. *Proteomics.* 11:2790–2797. https://doi.org/10.1002/pmic.201000800

Wais-Steider, J., and P. Satir. 1979. Effect of vanadate on gill cilia: switching mechanism in ciliary beat. *J. Supramol. Struct.* 11:339–347. https://doi.org/10.1002/jss.400110309

Wargo, M.J., and E.F. Smith. 2003. Asymmetry of the central apparatus defines the location of active microtubule sliding in *Chlamydomonas* flagella. *Proc. Natl. Acad. Sci. USA.* 100:137–142. https://doi.org/10.1073/pnas.0135800100

Wirschell, M., T. Hendrickson, and W.S. Sale. 2007. Keeping an eye on I1: I1 dynein as a model for flagellar dynein assembly and regulation. *Cell Motil. Cytoskeleton.* 64:569–579. https://doi.org/10.1002/cm.20211

Witman, G.B. 1986. Isolation of *Chlamydomonas* flagella and flagellar axonemes. *Methods Enzymol.* 134:280–290. https://doi.org/10.1016/0076-6879(86)34096-5

Witman, G.B. 1993. *Chlamydomonas* phototaxis. *Trends Cell Biol.* 3:403–408. https://doi.org/10.1016/0962-8924(93)90091-E

Witman, G.B., J. Plummer, and G. Sander. 1978. *Chlamydomonas* flagellar mutants lacking radial spokes and central tubules. Structure, composition, and function of specific axonemal components. *J. Cell Biol.* 76: 729–747. https://doi.org/10.1083/jcb.76.3.729

Yamamoto, R., K. Song, H.-A. Yanagisawa, L. Fox, T. Yagi, M. Wirschell, M. Hirono, R. Kamiya, D. Nicastro, and W.S. Sale. 2013. The MIA complex is a conserved and novel dynein regulator essential for normal ciliary motility. *J. Cell Biol.* 201:263–278. https://doi.org/10.1083/jcb.201211048

Yang, P., L. Fox, R.J. Colbran, and W.S. Sale. 2000. Protein phosphatases PP1 and PP2A are located in distinct positions in the *Chlamydomonas* flagellar axoneme. *J. Cell Sci.* 113:91–102.

Zhao, L., Y. Hou, T. Picariello, B. Craige, and G.B. Witman. 2019. Proteome of the central apparatus of a ciliary axoneme. *J. Cell Biol.* 218:2051–2070. https://doi.org/10.1083/jcb.201902017